Biophysical Journal, Volume *112*

Supplemental Information

Two Distinct Actin Networks Mediate Traction Oscillations to Confer Focal Adhesion Mechanosensing

Zhanghan Wu, Sergey V. Plotnikov, Abdiwahab Y. Moalim, Clare M. Waterman, and Jian Liu

Supporting Material S1 Text: Experiment Methods

1. Cell Culture, Transfection, and Reagents

Mouse embryo fibroblasts (MEFs) were provided by Dr. M. Beckerle (University of Utah) and were cultured in Dulbecco's modified Eagle's medium (DMEM) with high glucose supplemented with 15% fetal bovine serum (FBS), 2mM L-glutamine, 100U/ml penicillin/streptomycin, and non-essential amino acids at 37^0C, 5% CO2. The media and the supplements for the cell culture were purchased form Life Technologies. For experiments, the cells were transfected with 1μg of cDNAs encoding fluorescent fusion proteins by nucleofection by using cell line nucleofector kit V and program T20 (Lonza) according manufacture's protocol. cDNAs encoding paxillin-eGFP and actin-mApple were provided by Dr. M. Davidson (Florida State University). Transfected cells were cultured for 14-16hrs in plastic dishes as described above, than re-plated into glass–bottom imaging dishes (MatTek) and cultured for additional 4-6hrs in DMEM-FBS (10%) without phenol red. To promote cell attachment and integrin engagement, the surface of poly-lysine-coated imaging dishes (40ug/ml poly-D-lysine with MW 70-150kDa) was additionally treated with 10μg/ml of human plasma fibronectin (FN; EMD-Millipore) diluted in DPBS. The dishes were coated with FN for 2hrs at 37^oC and extensively washed with DPBS to remove unbound protein.

For partial inhibition of myosin ATPase activity, transfected cells cultured in imaging dishes were treated for 2hrs with 1μM blebbistatin (Toronto Research Chemicals). For formin inhibition, the cells were incubated for 4hrs with 10μM SMIFH2 or its inactive analog KV18 (Analog 7)(1) provided by Dr. D. Kovar (University of Chicago).

2. Time-lapse imaging and quantification of stress fiber elongation

For time lapse confocal imaging, MEFs were grown in fibronectin-coated imaging dishes (MatTek, see above) for 4hrs in DMEM-FBS (10%). Prior to imaging, the medium was changed to CO2-independent medium (DMEM-FBS supplemented with 10mM HEPES) and cell sample was mounted on an Eclipse Ti microscope (Nikon Instruments) equipped with a CFI Apo TIRF 60x N.A. 1.49 objective, a dynamic focusing system to correct for focus drift (PFS2; Nikon Instruments), a CSU-X1 confocal scanner (Yokogawa Electric Corporation), a CoolSnap HQ2 CCD video camera (Roper Scientific), and a dual galvanometer laser scanner (FRAPPA, Andor Technology). During the experiment the cells were maintained at 37C and at 85% humidity with a heated stage-top incubator and an objective heater (Pathology Devices). After the sample was mounted, the candidate cells for imaging were located by visual inspection using an epifluorescent mode of the microscope, and images of paxilllin-eGFP and actin-mApple were acquired to visualize FAs and stress-fibers. To investigate the dynamics of actin polymerization at the adhesion sites, individual stress fibers emanating from mature FAs were photo-labeled by bleaching two parallel lines across the stress-fiber. The spacing between bleached lines (1.2 μm) was determined empirically to create a bright spot with Gaussian profile of mApple intensity across it allowing us to locate the spot with sub-pixel accuracy (see Fig S8 for details). 45 images of actin-mApple were acquired at 1500ms time interval starting immediately after bleaching a photo-label on a stress-fiber. After the movie was taken an additional image of paxillin-eGFP was acquired to ensure that FA was stable (did not move, slide or disassemble) during the movie.

To determine the dynamics of stress-fiber elongation, movement of a photo-label on a stress-fiber was plotted as a *x-t* scan using a kymograph tool of the MetaMorph software (Molecular Devices). A line was drawn manually along a stress-fiber starting at the center of FA anchoring the stress-fiber, and a kymograph was generated by averaging intensity of mApple fluorescence over 0.75 μm line width. The position of a photo-label on a kymograph was tracked with sub-pixel accuracy by using the Gaussian fitting implemented by standard nonlinear regression of Matlab Statistics toolbox. The confidence intervals of the tracked positions are obtained by the regression parameter confidence interval estimator in Matlab Statistics toolbox. See Fig S8 for more details.

3. Analysis of actin retrograde flux

Retrograde flux of the actin network in cell lamellipodium (or right behind cell edge for CK-666 treated cells) and deep in the lamellum was performed by kymograph analysis. First, image sequences of mouse embryo fibroblasts expressing actin-mApple were acquired by spinning disk confocal microscope with 1.5s interval. Then, straight lines were drawn perpendicular to the closest cell edge and horizontal kymographs were created and analyzed by using kymograph tool in MetaMorph (Molecular Devices). Actin flux rate was calculated based on the angle of deflection from the horizontal direction.

4. High resolution traction force microscopy

High resolution traction force microscopy (TFM) was performed as described previously(2). Briefly, FN-coupled polyacrylamide (PAA) substrates with embedded 40nm red and far-red fluorescent beads were prepared on glass coverslips. Cells were plated on FN-coupled polyacrylamide substrates 2hrs prior to the experiment to minimize ECM deposition and remodeling. To modulate the shear modulus (G') of the substrate, the ratio of acrylamide to bisacrylamide was varied as described(3). Images of FAs labeled with eGFP-paxillin and the beads within the substrate were acquired by spinning disk confocal microscopy. The imaging system consisted of a Nikon TI inverted microscope equipped with the Perfect Focus system (Nikon Instruments), a CSU-X1 spinning disk confocal scan head (Yokogawa Electric Corporation), 100 mW 488 nm, 200 mW 561 nm and 100 mW 655 nm solid-state lasers (Spectral Applied Research), a CoolSNAP HQ2 camera (Roper Scientific), and a linear encoded motorized stage (Applied Scientific Instruments)(4). Temperature was controlled by an air stream (Nevtek) or stage top incubator (Pathology Devices). Images were acquired using a Plan Apo VC 60x WI N.A. 1.2 water immersion objective (Nikon Instruments) with additional 1.5X intermediate magnification. Up to 3 image triplets of eGFP-paxillin, red and far red fluorescent beads were captured in rapid succession at 1min intervals, then 5 ml of 0.5% phenol red-free trypsin-EDTA (Life Technologies) was perfused into the chamber to remove the cells from the PAA substrate, and an image of beads in the unstrained substrate was captured.

Correlation-based particle tracking velocimetry code in Matlab was used to quantify the cell-induced deformation of the PAA gel. Deformations were interpolated onto an 0.47μm displacement grid, and the stress field was reconstructed by Fourier-transformed traction cytometry and interpolated on a 0.47μm grid(2, 5, 6). To achieve high spatial resolution for traction maps, the regularization parameter did not exceed $2x10^{-6}$.

For simultaneous measurement of eGFP-paxillin intensity and traction magnitude across individual FAs we used a custom Matlab script. A line was drawn manually along the major

axis of a FA and the means of traction stress and eGFP-paxillin intensity were calculated within a 0.94x0.94μm window centered at every pixel along the line. Since precise segmentation of FAs is challenging due to the sensitivity of locating the FA borders to the fluorescence intensity of the image, we detected the pixel along this line with maximal eGFP-paxillin intensity and considered it as the center of the FA. The shift of the position of peak traction from the FA center was considered positive if it was shifted from center towards the distal tip of FA (towards the leading edge).

To analyze total force exerted by a cell on the ECM, a binary cell mask was created by intensity thresholding of eGFP-paxillin images and dilated by 50 pixels to include vectors that enter the region of interest (ROI), but whose origins lay just outside the ROI. Traction vectors outside the cell were defined as background forces and only vectors whose magnitudes ≥ 2x greater than background were included in the analysis. The sum of traction stresses per unit area was calculated and multiplied by the area of either a FA or the entire cell(7).

5. Immunofluorescence

Cells were plated on FN-coated glass coverslips for 24hrs, washed in warm PBS, fixed in 4% paraformaldehyde followed by permeabilization with 0.25% Triton X-100. The cells were blocked in 2% BSA, incubated with primary antibodies for 1hr, washed in PBS-0.1% Tween-20, and incubated with fluorophore-conjugated secondary antibodies (Jackson ImmunoResearch Laboratories). AlexaFluor488–phalloidin (Invitrogen) was included in the secondary antibody solution. The coverslips were mounted on microscope slides in Fluoroshield mounting media (Sigma-Aldrich), and sealed with nail polish. Primary antibodies used were as follows: monoclonal anti-vinculin (1:200) and anti-talin (1:100; Sigma-Aldrich); monoclonal anti-paxillin (1:100) and anti-FAK (1:100; BD Biosciences); monoclonal anti-tensin (1:100; Santa Cruz Biotechnology); rabbit polyclonal anti-phospho-FAK pTyr397 (1:100; Invitrogen); rabbit polyclonal anti-cortactin (1:100; Cell Signaling Technology). The cells were imaged on an inverted microscope (Nikon Ti, 60x, 1.4 NA objective) using a CoolSNAP MYO CCD camera (Roper Scientific).

6. Statistical analysis details on stress fiber elongation oscillation

The criteria to detect oscillations in SF elongation rate states as follows: if there are at least three significant peaks in the time course of SF elongation rate in a row, the corresponding FA is counted as FA with SF elongation rate oscillation. The average elongation rate oscillation magnitude is calculated as $\Delta v_{SF} \cdot t_{oscill} / t_{tot}$, where Δv_{SF} is the sum of the SF elongation rate oscillation magnitude during the oscillating period (t_{oscill}), and t_{tot} is the total SF elongation time during the measurement. This term therefore has the unit of nm/s. The significant peaks are defined as: The peaks in velocity vs. time plot which is larger than the maximum noise level based on the error estimations from 95% confidence interval of Gaussian fitting of Kymographs, CramerRao bound estimation from background measurements outside of SF area, and the fixed cell measurements.

7. Details of theoretical model

Details on the construction and implementation of the theoretical model and the supplemental figures are in the Supporting Material S3 Text.

References

1. Rizvi, S. A., E. M. Neidt, J. Cui, Z. Feiger, C. T. Skau, M. L. Gardel, S. A. Kozmin, and D. R. Kovar. 2009. Identification and Characterization of a Small Molecule Inhibitor of Formin-Mediated Actin Assembly. Chemistry & Biology 16:1158-1168.
2. Sabass, B., M. L. Gardel, C. M. Waterman, and U. S. Schwarz. 2008. High Resolution Traction Force Microscopy Based on Experimental and Computational Advances. Biophysical Journal 94:207-220.
3. Yeung, T., P. C. Georges, L. A. Flanagan, B. Marg, M. Ortiz, M. Funaki, N. Zahir, W. Ming, V. Weaver, and P. A. Janmey. 2005. Effects of substrate stiffness on cell morphology, cytoskeletal structure, and adhesion. Cell Motility and the Cytoskeleton 60:24-34.
4. Shin, W. D., R. Fischer, P. Kanchanawong, Y. Kim, J. Lim, K. Myers, Y. Nishimura, S. V. Plotnikov, I. Thievessen, D. Yarar, B. Sabass, and C. M. Waterman. 2010. A versatile, multi-color total internal reflection fluorescence and spinning disk confocal microscope system for high-resolution live cell imaging. In Live Cell Imaging: A Laboratory Manual. R. D. Goldman, J. R. Swedlow, and D. L. Spector, editors. Cold Spring Harbor Laboratory Press, Cold Spring Harbor, NY. 119-138.
5. Gardel, M. L., B. Sabass, L. Ji, G. Danuser, U. S. Schwarz, and C. M. Waterman. 2008. Traction stress in focal adhesions correlates biphasically with actin retrograde flow speed. The Journal of Cell Biology 183:999-1005.
6. Schwarz, U. S., N. Q. Balaban, D. Riveline, A. Bershadsky, B. Geiger, and S. A. Safran. 2002. Calculation of Forces at Focal Adhesions from Elastic Substrate Data: The Effect of Localized Force and the Need for Regularization. Biophysical Journal 83:1380-1394.
7. Maruthamuthu, V., B. Sabass, U. S. Schwarz, and M. L. Gardel. 2011. Cell-ECM traction force modulates endogenous tension at cell,Äìcell contacts. Proceedings of the National Academy of Sciences.

Supporting Material S2 Text: Supporting movie captions

Movie S1. Model simulation result showing FA growth from nascent stage coupled with membrane protrusion.

Movie S2. FA traction peak oscillation in time and space. Above: a typical model result. Below: experiment observation. The red dots represent the location of the FA traction maximum.

Movie S3. Temporal evolution of the FA traction profile during the FA traction peak oscillation. Above: a typical model result. Below: experiment observation. The FA traction profiles in both movies are along the centerline in the long-axis of the FA.

Supporting Material S3 Text: Model equations, model parameters, additional model phase diagram studies, supplemental figures, and supplemental references

Zhanghan Wu[1, #], Sergey V. Plotnikov[3, #], Abdiwahab Moalim[3], Clare M. Waterman[2] and Jian Liu[1, *]

1. Theoretical Cellular Physics Section, BBC,
2. Laboratory of Cell and Tissue Morphodynamics, CBPC,
National Heart, Lung, and Blood Institute, NIH, Bethesda, MD 20892
3. Department of Cell and Systems Biology, University of Toronto, Toronto, ON M5S 3G5, Canada

(#) Equal contribution

(*) Corresponding authors: jian.liu@nih.gov

I. Model Equations

The model aims to provide a realistic picture of FA growth and traction force generation based on many well-established experimental observations. It describes the spatial-temporal evolution of FA growth that responses to, and acts upon actin dynamics; the mechanochemical coupling hereby orchestrates the distinct spatial patterns of traction force and biochemical signals within the FA. Below we first provide the overall qualitative picture of the model, and then present the mathematical equations in details.

1. Qualitative model essence

As FA is a well-layered structure(1), we built our integrated model on the level of four structural functional modules: Extracellular matrix (E), Integrins (I), Adaptor proteins (A), and Actin cytoskeletons. Based on the layered structure, these functional modules only interact with their neighboring layers. In addition, there are two signaling functional modules: protein tyrosine kinases (PTK) and phosphatases (PTP). Depicting FA on the level of functional modules is a simplification that allows us to look beyond roles of individual molecular players and discern the collective behavior between functional modules on system level.

The model envisions the following dynamic process of FA growth (see Fig. 1 and S1), beginning from a small cluster of the ECM-integrin-adaptor mechanical linkages (E-I-A) that occupy an area $\sim$ 200nm in diameter and are in chemical equilibrium with E-I, I-A, I, A. In addition, there are high PTK activity and low PTP activity in the small domain. These initial elements constitute the nascent FA. The branched actin network polymerizes at the cell membrane, resulting in a combination of the membrane protrusion and the retrograde actin flux. The mechanical interaction between the actin flux and the FA is reciprocal: It stretches the E-I-A linkage, and in turn slows down the actin flux. Upon stretching, the adaptor proteins, which are molecular clutches, further strengthen the E-I-A linkage by recruiting more adaptors and integrins. When the stretch is too large, it breaks the bonds in the E-I-A linkage, resulting in the disengaged FA components I-A, E-I, and A. In particular, the disengaged I-A and A will drift with the retrograde actin flux, and promote the downstream directional FA growth. At this stage, the FA traction consequently tapers off from the more anchored FA frontal tip toward the more drifting proximal end. As the PTK within the FA is mechanosensitive(2), its spatial profile thus mirrors that of the traction force and affects the FA-localized signal cascades in two ways. First, it potentiates actin-adaptor interaction and strengthens the mechanical linkage near the FA frontal end where the traction force is higher, thus underlies a positive feedback. Second, because the PTK is in antagonism with protein tyrosine phosphatase (PTP), PTK functional module is suppressed in the newly acquired FA area where the traction force is lower. Consequently, the Rho-mediated pathway downstream of the PTP can get activated and actomyosin contractility can impinge upon the FA near its proximal end. Finally, the actomyosin contraction promotes actin polymerization from the plus end of the stress fiber. This actin polymerization relaxes the contractility, acting as a negative feedback that regulates the actomyosin contractility and FA traction force.

Before delving into the detailed mathematical depictions of our model, we would like to further emphasize the necessity of the realistic description of mechanics and

biochemistry pertaining to the layered structure and the growth of FA. By the same token, we also compare our model with the simplified models proposed by others. This comparison renders the essential features of our model more self-evident.

The central theme of our paper hinges on the synergy between theory and experiments, which together provides a coherent model for FA growth. To faithfully compare with our *in vivo* experiment results, the model therefore needs to be realistic. This entails the model to organically integrate multiple known factors essential for FA growth and mechanosensing based on experiments. In contrast, each of the previous models by other researchers focuses on a specific aspect of FA dynamics, and studies these individual effects in details. Theoretical exercises along this line have proven fruitful, but fall short of the goal in this paper. Below, as an example, we discuss the common features shared by, and the difference between, our model and Sabass and U Schwarz's model (3).

Sabass and Schwarz model investigates the mechanical interaction between moving F-actin and stationary FA. It assumes a constant force pulling an actin filament to pass overhead the FA, which is modeled as a stationary geometric entity without dimension. There are two sources of forces that counterbalance this constant driving force. First, an elastic force arises when the FA binds to the moving F-actin that subsequently stretching the bond. Second, a frictional force stems from the immersion of the F-actin in the actin meshwork. Importantly, the off rate of FA-actin bond increases with the elastic stretching, like a slip-bond. Depending on bond dynamics and the frictional drag of F-actin with the actin meshwork, this model reveals a number of interesting phenomena and could explain the observed biphasic dependence of FA traction force on actin flow rate.

Similarity: Our model also assumes force balance (see Fig S1), describes the similar slip-bond behavior of FA, and can recapitulate the observed biphasic dependence of FA traction force on actin flow rate.

Key Differences:

1. Our model does not assume a constant pulling force that drives the actin retrograde flow, as we do not have experimental evidence for this constant force in our own system. Instead, the model describes a constant actin polymerization rate at the cell leading edge. This is based on the observation that the total actin polymerization rate is conserved, as the sum of the cell front protrusion speed and retrograde actin flow rate remains roughly constant during cell spreading and cell migration (4). Consequently, the resistance of the membrane elasticity against membrane protrusion constitutes the driving force for the retrograde actin flow at the boundary. Additionally, the mechanical interaction with FA locally slows down the retrograde actin flow. It is the pressure arising from the resulting spatial variation of the actin flow field that pushes the membrane forward. That is, the FA provides the anchorage for the actin polymerization to push the membrane efficiently. This is consistent with the observation that disrupting the actin-FA engagement inhibits the cell front protrusion and increases the retrograde actin flow (*e.g.*, (5)).

2. Because experiments show that FA adaptor proteins (*e.g.*, talin) under stretching expose more binding sites for integrin and actin (*e.g.*, (6)), the model explicitly incorporates this catch-bond behavior of FA, which is not described in Sabass and Schwarz's work. Together with the FA slip-bond behavior, our model can recapitulate the biphasic dependence of FA traction force on actin flow rate evidenced in experiments (see Fig S2). In

fact, recent experiments show that this mechanosensitivity of talin and its binding partner, vinculin, is essential for strengthening ECM-FA linkage in Human foreskin fibroblasts, HeLa cells, and CV1 cells (5, 7).

3. Our model describes FA as a composite concentration field of different species. This depiction is in accordance to the layered structure of FA evidenced in experiments. From bottom to top, they are ECM, integrin, adaptor, and actin cytoskeleton. Here, force is balanced for each layer (Fig S1). Importantly, the mobile FA species in our model, e.g., the free adaptor proteins, can drift with retrograde actin flow as evidenced in experiment (*e.g.*, (8)). During drifting, these mobile FA species are assumed to be capable of binding with F-actin and integrin, thus contributing to the FA centripetal growth. This depiction is closer to reality and enables us to systematically study FA growth (Figs S2-S4, S6-7). More crucially, we showed that the FA structural plasticity arising from FA layered structure and growth dynamics directly underlay efficient FA mechanosensing (Fig. S10). Our model therefore goes beyond the previous models, in which FA is modeled as a dimensionless entity without growth or shrinkage.

2. Mathematical equations

Below, we formulated the qualitative model into mathematical equations. As the LP is much thinner (~200nm) than its other two dimensions and the height of the cell itself, we simplified the problem as quasi-2D problem in the x-y plane, in which the membrane protrusion is pre-defined in the negative direction of the x-axis. Additionally, the model only described the mechanical effects of actin networks on and reciprocal action from FA and membrane without explicit representations of the geometries of branched actin network and SF formation.

We solved the coupled partial differential equations (PDEs) by the finite element solver COMSOL Multiphysics software (version 4.3). The time dependent solver was used with relative tolerance of 5×10^{-4}. The BDF (backward differentiation formula) method was used for time stepping provided by default Multiphysics module of COMSOL. The solver used is MUMPS (multifrontal massively parallel sparse direct solver) also from default Multiphysics module of COMSOL.

(2.1) Dynamics of retrograde actin flux

Retrograde actin flux is modeled as a Navier-Stokes hydrodynamic flow. Branched actin network is viscoelastic (*e.g.*, (9-12)), which is more viscous fluid-like during FA growth. This is because the actin meshwork in cell leading edge constantly undergoes remodeling, the timescales of which relate to the lifetimes of F-actin itself and the associated crosslinking proteins. Most crosslinking proteins have lifetimes of ~ 1 – 10 seconds (*e.g.*, (13, 14)), while F-actin itself in LP has lifetime of ~ 10 – 20 seconds (*e.g.*, (13-15)). Therefore, the stress exerted upon actin network is expected to dissipate at timescale > 10s seconds, over which the actin network effectively behaves like a fluid. This conclusion is indeed supported by experimental measurements (*e.g.*, (9-12)). On the other hand, FA growth typically takes minutes, much longer timescale than the lifetimes of F-actin and the crosslinkers. Due to this timescale separation, the retrograde actin flow behaves more like a viscous flow during FA growth. We also note that actin meshwork alone might retain some

weak residual elastic response at the long timescales (*e.g.*, (9, 11)), although the entire cytoplasm *in vivo* has been demonstrated to be a liquid at long timescales with the elastic modulus approaching zero (16). However, since the typical values of such residual elastic modulus of the branched actin network are ~ 10 Pa or smaller << the FA traction in our system (~1 kPa), this residual elasticity is expected to play a very minor role in the FA force generation and hence is ignored in the model. We therefore approximated the dynamics of the actin flux by Navier-Stokes hydrodynamics (Eqs. (S1)-(S3)).

Eq. (S1) describes the dynamics of actin flow velocity field influenced by the impinging stress from its spatial gradient and the FA-actin flux engagement.

$$\rho \frac{\partial \vec{\mathbf{v}}_{actin}}{\partial t} = \nabla \cdot \left(-p\mathbf{I} + 2\eta \mathbf{D} - \frac{2}{3}\eta (\nabla \cdot \vec{\mathbf{v}}_{actin})\mathbf{I} \right) - \vec{F}_{adh} \tag{S1}$$

where $\vec{\mathbf{v}}_{actin}$ is the actin velocity field; ρ is F-actin density; p is actin pressure as a fluid; $\mathbf{I}$ is the unit tensor; $\mathbf{D} = \frac{1}{2}\left[\nabla \vec{\mathbf{v}}_{actin} + \nabla \vec{\mathbf{v}}_{actin}^{\,T} \right]$ is strain rate tensor; η is the dynamic viscosity of actin flux; and $\vec{F}_{adh}$ is the actin flux-mediated FA traction transmitted onto the ECM, which reciprocally resists the actin flux (the minus sign). As the system is in low-Reynolds number limit, the model ignores the inertial term in Navier-Stokes equation (Eq. (S1)).

Eq. (S2) recapitulates the dynamics of F-actin mass density, in which the actin flux is modeled as a compressible flow. Experiments demonstrate that the majority of branched actin network depolymerization occurs at the LP/LM interface (17). This effect is essentially treated as a boundary condition (Eq. (S2)).

$$\frac{\partial \rho}{\partial t} + \nabla \cdot \left(\rho \vec{\mathbf{v}}_{actin} \right) + k_\rho \rho = 0 \tag{S2}$$

where k_ρ is actin depolymerization rate that peaks near the LP/LM interface $k_\rho(x,y) = k_\rho^{(0)} \exp\left(-\left(\frac{y - y_0}{L_{P/M}} \right)^2 \right)$, $k_\rho^{(0)}$ is the maximum actin depolymerization rate, y_0 and $L_{P/M}$ are the vertical coordinate and the characteristic width of the LP/LM interface, respectively. We choose $L_{P/M}$ =250 nm in typical simulations; varying $L_{P/M}$ between 100 nm and 1 μm does not critically affect the model result. The initial F-actin mass density in the model simulation (Eqs. (S1) and (S2)) is set to be the measured bulk density of F-actin in LP, ρ_0 (see parameter table). The F-actin depolymerization is an essential ingredient of FA growth model, because the pool of actin monomers is always finite in migrating cells. The F-actin depolymerization at LP/LM interface is an integral part of the "tread-milling mechanism" (18), which by active transport provides a steady supply of actin monomers for the branched actin network polymerization at the leading edge (*e.g.*, (19, 20)). The model presents a simplified description of the actin dynamics in LP and at LP/LM. Specifically, the model assumes a constant polymerization rate of branched actin network at the cell membrane, and imposes a fixed width of LP, while the majority of F-actin depolymerization

occurs at LP/LM interface. This model treatment implicitly assumes that the actin monomers releasing from F-actin depolymerization recycle to the cell leading edge, thus maintaining a constant pool of actin monomers. Given the finite pool of actin monomers *in vivo*, the absence of the F-actin depolymerization at LP/LM interface in the model will dictate a gradual decrease in the polymerization rate of branched actin network at the cell membrane during FA growth and the coupled membrane protrusion, as the available actin monomers become less and less.

Eq. (S3) is the state equation for the pressure arising from actin flux p:

$$\Delta p = \nabla\left(2\eta\mathbf{D} - \frac{2}{3}\eta\left(\nabla\cdot\vec{\mathbf{v}}_{actin}\right)\mathbf{I}\right) - \nabla\vec{F}_{adh} \tag{S3}$$

It is this pressure from actin flux that reciprocally acts as a thrust protruding the membrane (see the subsection (2.2) below). The membrane constitutes the moving boundary of the actin flux. Due to the conservation of the total amount of the actin polymerization, this boundary condition set the actin flux velocity at the membrane to be $V_{flux}=V_0-V_{membrane}$ (pointing toward to positive direction of x-axis). This way, the evolving actin flow field in the model therefore arises from solving the coupled Eqs. (S1)-(S3), in conjunction with solving the membrane dynamics and actin flux-FA engagement.

(2.2) Membrane dynamics and its interplay with actin flux

The dynamic equation of cell membrane can be written as

$$\lambda_m \frac{\partial h(x,t)}{\partial t} = -\frac{\delta H\left(h(x,t)\right)}{\delta h(x,t)} + \zeta(x,t) \tag{S4}$$

H is the Helfrich free energy intrinsic to the membrane, h(x, t) is the membrane height in the negative direction of x-direction under Monge Gauge, representing the membrane shape over time and space. λ_m is damping factor characterizing membrane resistance and fluid drag outside. $\zeta(x,t)=f-f_e$ is the external force impinging upon the membrane, where f is the protruding stress exerted by the branching actin network, and f_e characterizes the effective resistance from the rest of the cell membrane that prevents the membrane protrusion. Here, the Helfrich membrane free energy is $H=\int_{\Omega} d\vec{\mathbf{r}}\left(\frac{\kappa_m}{2}[\Delta h]^2+\frac{\sigma_m}{2}[\nabla h]^2\right)$, where κ_m is bending energy coefficient and σ_m is tension energy coefficient. Together, the membrane dynamic equation can be written as:

$$\lambda_m \frac{\partial h(x,t)}{\partial t} = \zeta(x,t) - \kappa_m \frac{\partial^4 h}{\partial x^4} + \sigma_m \frac{\partial^2 h}{\partial x^2} \tag{S5}$$

Note that we treated the membrane as a moving boundary for the actin flux. Following the Navier-Stokes equations (Eqs. (S1–S3)), the stress upon the actin flux that gives rise to the local flux velocity $\vec{\mathbf{v}}_{actin}$ at the membrane is

$T|_{membrane} = \left(-p\mathbf{I} + 2\eta\mathbf{D} - \frac{2}{3}\eta(\nabla \cdot \vec{\mathbf{v}}_{actin})\mathbf{I} \right)\Big|_{membrane}$. Due to force balance, this stress has to stem from the membrane; reciprocally, the stress *f* exerted by the actin flux on the membrane is $f = -T|_{membrane}$. Moreover, while the actin flux velocity field is solved by the Navier-Stokes hydrodynamics, it is controlled by two additional factors. They are: (1) F-actin is depolymerized at the LP/LM interface; (2) the FA locally exerts resistant force (-$\vec{F}_{adh}$) against the actin flux. To jump-start the simulation, we introduced a uniform field of actin flux at t=0 sec at the membrane, reflecting a conserved polymerization rate of branched actin network over time (k_p). This initial actin flux will invoke $-\vec{F}_{adh}$upon engaging with the nascent FA; the resulting resistance slows the local velocity as well as the entire field of actin flux, which consequently generates the nonzero protruding stress $f = -\left(-p\mathbf{I} + 2\eta\mathbf{D} - \frac{2}{3}\eta(\nabla \cdot \vec{\mathbf{v}}_{actin})\mathbf{I} \right)\Big|_{membrane}$ pushing the membrane forward. In this sense, the protrusion stress (*f*) by the actin here implicitly depends on the FA-actin flux engagement. We showed that only after engaging with the FA, could the actin polymerization efficiently drive the membrane protrusion and FA growth (Figs 2A and S2). This model feature is an integral part of the FA growth dynamics, and is consistent with experimental observations (*e.g.*, (5)).

(2.3) Convection-diffusion-reaction in FA growth

The model describes FA growth dynamics by three processes: diffusions and the actin flux-driven drifting of FA mobile components, and chemical reactions. The chemical reactions include (1) the FA-localized kinase-phosphatase interactions, and (2) the inter-conversions of these FA mobile components among themselves and with the fully anchored FA component according to the layered structure (see the FA constitutive reaction scheme in Fig. 1G). For example, the chemical reaction of $E - I + A$ $E - I - A$ describes that ECM–integrin–adaptor linkage (E–I–A) forms from, and breaks into, ECM–integrin (E–I) and adaptor (A). Among FA components, only the ECM (E) or ECM-anchored FA components, *i.e.*, ECM–integrin (E–I) and ECM–integrin–adaptor (E–I–A), cannot drift with actin flux. All the other FA components are mobile and can undergo 2D diffusion and convection with actin flux. Here, chemical reactions comply with mass balance, and follow the Michaelis-Menten like kinetics. Consequently, when the bonds in E–I–A break, the disengaged FA species (*e.g.*, "A") drifts with actin flux. While this convectional removal of "A" shifts the local chemical equilibrium toward more disintegration of E–I–A, this drifting "A" could bind to integrin and hence become anchored onto ECM, thus depositing downstream. Similar processes also apply other FA-localized bond breaking and rebinding events, which promote the elongated FA growth.

In the model, the local levels of FA components are 2D densities that are coarse-grained by the spatial resolution ~ 30 nm, and then further normalized to the maximum occupancy, *e.g.*, [E–I–A]+[E–I]+[E]=1. The reported spatial profile of FA domain is the sum of E–I–A, E–I, and I–A. Assuming force balance (Fig. S1), the local traction force modulates these reaction rates (*i.e.*, catch/slip bonds), which impact the FA growth that in turn further influence the mechanical interaction with actin cytoskeleton. This way, the FA growth model integrates mechanics and biochemistry. In general, the FA shape arises from the balance between diffusion, convection, and reactions pertaining to FA assembly, although

an extremely fast actin flux could cause overwhelming removal of FA mobile components and eventually wash away the entire FA in the model.

(2.3.1) "E–I–A" dynamics:

$$\frac{\partial EIA}{\partial t} = \underbrace{\left(k_+^{(0)} + k_{+F}^{(0)} \frac{\left(F_{EIA}/F_0\right)^{n_0}}{1+\left(F_{EIA}/F_0\right)^{n_0}} \right) \cdot EI \cdot A}_{\text{Conversion from EI and A to EIA}} + \underbrace{\left(k_+^{(1)} + k_{+F}^{(1)} \frac{\left(F_{EIA}/F_0\right)^{n_0}}{1+\left(F_{EIA}/F_0\right)^{n_0}} \right) \cdot \left(1 - EI - EIA\right) \cdot IA}_{\text{Conversion from IA to EIA}} - \underbrace{\left(k_-^{(0)} \cdot e^{\frac{F_{EIA}^2}{2 s_1 k_B T}} + k_-^{(1)} \cdot e^{\frac{F_{EIA}^2}{2 s_1 k_B T}} \right) \cdot EIA}_{\text{Conversion from EIA to (E+ IA) and (EI+A)}} \quad \text{(S6)}$$

The catch-bond behavior is modeled by force-dependent formation rates of E–I–A. The force on E–I–A is $F_{EIA} = \underbrace{\xi \cdot \left|\vec{\mathbf{v}}_{actin}\right| \cdot EIA}_{\text{Viscous drag force}} - \underbrace{\eta_s \cdot \left(\nabla \cdot \vec{\mathbf{v}}_{actin}\right) \left| \frac{\vec{\mathbf{v}}_{actin}}{\left\|\vec{\mathbf{v}}_{actin}\right\|} \right| \cdot EIA}_{\text{Shear stress}} + \underbrace{f_{\max} \cdot M}_{\text{Contractility}}$ (see Eqs. (S13) and (S16) for details). $k_{+F}^{(0)} \frac{\left(F_{EIA}/F_0\right)^{n_0}}{1+\left(F_{EIA}/F_0\right)^{n_0}}$ and $k_{+F}^{(1)} \frac{\left(F_{EIA}/F_0\right)^{n_0}}{1+\left(F_{EIA}/F_0\right)^{n_0}}$ recapitulate the observed catch-bond behaviors: The more the adaptor gets stretched, the more it extends and exposes more binding sites that mediate further adaptor and integrin recruitment (6, 21, 22). Specifically, the stretched adaptor A in the E–I–A recruits another adaptor A, which will provide the dock sites for E–I to form more E–I–A (the $k_{+F}^{(0)}$ term). Alternatively, the stretched adaptor A in the E–I–A can directly recruit I–A, which binds to the unoccupied ECM (E) to form the new E–I–A (the $k_{+F}^{(1)}$ term). The force-dependences in the above formula phenomenologically reflect the nonlinear response of the adaptor extension upon force (6). While β1 integrin also exhibits catch bond behaviors upon tension (21), the threshold force to activate such molecular clutch is ~ 20 pN (21), >> 1-3pN per integrin involved here. The model therefore neglected the contribution of integrin in catch bonds.

The slip-bond behavior is modeled by force-dependent disassembly rate of E–I–A. That is, the force builds up strain energies in the E-I-A linkage and hence weakens its stability. The linkage can be represented by a series of connected springs, whose effective spring constant is $s_1 = \frac{E_0 E}{E_0 + E}$. E is the ECM stiffness and E_0 is the effective spring constant

for the FA, which is mainly attributed to the I–A in the fully anchored E–I–A. The stored strain energy is thus $\frac{F_{EIA}^2}{2s_1}$, which exponentially increase the dissociation rates according to the Bell model (23), *i.e.*, E–I–A exhibits slip-bond behavior via the force-dependent off rates $k_-^{(0)}e^{\frac{F_{EIA}^2}{2s_1k_BT}}$ and $k_-^{(1)}e^{\frac{F_{EIA}^2}{2s_1k_BT}}$ that break the E–I–A into E and I–A, and E–I and A, respectively (24).

(2.3.2) "E–I" dynamics:

$$\frac{\partial EI}{\partial t} = \underbrace{k_+^{EI}\cdot I\cdot(1-EI-EIA)}_{\text{Conversion from I to EI}} + \underbrace{k_-^{(0)}\cdot e^{\frac{F_{EIA}^2}{2s_1k_BT}}\cdot EIA}_{\text{Conversion from EIA to EI}} - \underbrace{k_-^{EI}\cdot EI}_{\text{Conversion to E and I}} - \underbrace{\left(k_+^{(0)}+k_{+F}^{(0)}\frac{\left(F_{EIA}/F_0\right)^{n_0}}{1+\left(F_{EIA}/F_0\right)^{n_0}}\right)\cdot EI\cdot A}_{\text{Conversion from EI and A to EIA}} \quad \text{(S7)}$$

(2.3.3) "I–A" dynamics:

$$\frac{\partial IA}{\partial t} = \underbrace{D_{IA}\cdot\nabla^2 IA}_{\text{Diffusion of IA}} + \underbrace{k_+^{IA}\cdot I\cdot A}_{\text{Conversion from I and A}} + \underbrace{k_-^{(1)}\cdot e^{\frac{F_{EIA}^2}{2s_1k_BT}}\cdot EIA}_{\text{Conversion from EIA to IA}} - \underbrace{k_-^{IA}\cdot IA}_{\text{Conversion to I and A}} - \underbrace{\left(k_+^{(1)}+k_{+F}^{(1)}\frac{\left(F_{EIA}/F_0\right)^{n_0}}{1+\left(F_{EIA}/F_0\right)^{n_0}}\right)\cdot\left(1-EI-EIA\right)\cdot IA}_{\text{Conversion from IA to EIA}} - \underbrace{\vec{\mathbf{v}}_{IA}\cdot\nabla IA}_{\text{IA drifting with the actin flux}} \quad \text{(S8)}$$

where $\vec{\mathbf{v}}_{IA}=\alpha_{IA}\vec{\mathbf{v}}_{actin}$ and α_{IA} are the drift velocity and drifting coefficient of I–A with the actin flux $\vec{\mathbf{v}}_{actin}$.

(2.3.4) "I" dynamics:

$$\frac{\partial I}{\partial t} = \underbrace{D_I\cdot\nabla^2 I}_{\text{Diffusion of I}} + \underbrace{\left(k_{r_E}^I\cdot E+k_{r_A}^I\cdot A\right)\cdot(1-EIA-EI-IA-I)}_{\text{Recruitment by A and E}} + \underbrace{k_-^{IA}\cdot IA}_{\text{Conversion from IA}} + \underbrace{k_-^{EI}\cdot EI}_{\text{Conversion from EI}} - \underbrace{k_+^{EI}\cdot I\cdot(1-EI-EIA)}_{\text{Conversion to EI}} - \underbrace{k_+^{IA}\cdot I\cdot A}_{\text{Conversion to IA}} - \underbrace{k_-^{I}\cdot I}_{\text{Turn over of I into cytoplasm}} \quad \text{(S9)}$$

The "*E*" here refers to the free ECM that is not bound to integrins, nor integrin-adaptor complexes. The intrinsic integrin recruitment rate by the ECM must be very small *in vivo* 2D case; otherwise, activated integrins bound to the ECM will cover entire ventral surface during cell adhesion. The model thus sets the term for integrin recruitment by the free ECM to zero, *i.e.*, $k_{r_E}^I = 0$ for simplification. A very small value of $k_{r_E}^I$ will not affect the model result. Additionally, the free "I" cannot drift with the actin flux, as it is not in direct contact with the actin flux.

(2.3.5) "A" dynamics:

$$\frac{\partial A}{\partial t} = \underbrace{D_A \cdot \nabla^2 A}_{\text{Diffusion of A}} + \underbrace{k_{r_I}^A \cdot (I + EI) \cdot (1 - EIA - IA - A)}_{\text{Recruitment by I and EI}} + \underbrace{k_-^{IA} \cdot IA}_{\text{Conversion form IA}} + \underbrace{k_-^{(0)} \cdot e^{\frac{F_{EIA}^2}{2s_1 k_B T}} \cdot EIA}_{\text{Conversion from EIA}}$$

$$- \underbrace{\left(k_+^{(0)} + k_{+F}^{(0)} \frac{\left(F_{EIA}/F_0\right)^{n_0}}{1 + \left(F_{EIA}/F_0\right)^{n_0}} \right) \cdot EI \cdot A}_{\text{Conversion to EIA}} - \underbrace{k_+^{IA} \cdot I \cdot A}_{\text{Conversion to IA}} - \underbrace{k_-^A \cdot A}_{\text{Turn over of A into cytoplasm}} - \underbrace{\vec{\mathbf{v}}_A \cdot \nabla A}_{\text{Drift of A with the actin flux}}$$

(S10)

where $\vec{\mathbf{v}}_A = \alpha_A \vec{\mathbf{v}}_{actin}$ and α_A are the drift velocity and drifting coefficient of free *A* with the actin flux $\vec{\mathbf{v}}_{actin}$.

(2.3.6) "PTK" and "PTP" dynamics:

$$\frac{\partial K}{\partial t} = \underbrace{D \cdot \nabla^2 K}_{\text{Diffusion of PTK}} + k_+^K \cdot \underbrace{\frac{F_{EIA}}{F_{MK} + F_{EIA}}}_{\text{Mechanosensitive response of PTK activity}} \cdot \underbrace{\left(\frac{1}{1 + \left(P/\beta_P\right)^{n_P}} \right)}_{\text{PTP inhibition}} \cdot (1 - K) - \underbrace{k_-^K \cdot K}_{\text{Turn over of PTK activity}}$$

(S11)

$$\frac{\partial P}{\partial t} = \underbrace{D \cdot \nabla^2 P}_{\text{Diffusion of PTP activity}} + k_+^P \cdot \underbrace{\left(\frac{1}{1 + \left(K/\beta_K\right)^{n_K}} \right)}_{\text{PTK inhibition}} \cdot (EIA + IA) \cdot (1 - P) - \underbrace{k_-^P \cdot P}_{\text{Turn over of PTP activity}}$$

(S12)

K and *P* denote the activities of PTK and PTP, respectively, and are in mutual inhibition (25-27). According to the observations that PTP needs to bind with the FA-bound adaptor proteins (e.g., paxillin) to exert phosphatase activities (28), the activation of PTP in the model is set to be proportional to the sum of the local levels of E–I–A and I–A. In addition, β_P is the threshold activity above which PTP inhibition on PTK becomes significant, and β_K is the counterpart for PTK.

(2.4) Actin flux-mediated FA traction force

The actin flux-mediated FA traction force includes the viscous drag due to the relative velocity of actin flux with the FA, and the shear stress due to the actin flux velocity gradient, which causes the local deformation of the FA.

$$\vec{F}_{adh} = \underbrace{\xi \cdot \vec{\mathbf{v}}_{actin} \cdot EIA + \eta \cdot (\vec{\mathbf{v}}_{actin} - \vec{\mathbf{v}}_{IA}) \cdot IA + \eta \cdot (\vec{\mathbf{v}}_{actin} - \vec{\mathbf{v}}_{A}) \cdot A}_{\text{Viscous drag force}} - \underbrace{\eta_s \cdot \left(\nabla \cdot \vec{\mathbf{v}}_{actin}\right) \frac{\vec{\mathbf{v}}_{actin}}{\left\|\vec{\mathbf{v}}_{actin}\right\|} \cdot EIA}_{\text{Shear stress}} \tag{S13}$$

$$\xi = \underbrace{\xi_0 \cdot \frac{E}{E + E_0} \cdot \frac{K^2}{K_{0\xi}^2 + K^2}}_{\substack{\text{Additional viscous darg coefficient} \\ \text{from binding/unbinding events with FA}}} + \underbrace{\eta}_{\substack{\text{Intrinsic viscosity} \\ \text{of actin flux}}} \tag{S14}$$

Here, ξ is the viscous drag coefficient between actin flux and FA, η is the dynamic viscosity of the actin flux, and the η_s is the shear stress coefficient of FA that is attributed to the fully anchored E-I-A. $\frac{\vec{\mathbf{v}}_{actin}}{\left\|\vec{\mathbf{v}}_{actin}\right\|}$ is the unit vector of the local actin flux, which is zero if the actin flux is zero. While the actin flux itself has its own viscosity, its transient binding/unbinding with the fully anchored E–I–A introduces an additional viscous drag. In this context, we took the advantage of the recent theoretical work, which showed that such additional viscous drag coefficient is defined by spring constant of the E-I-A linkage ($s_1 = \frac{E_0 \cdot E}{E_0 + E}$) times the lifetime of the bond between E–I–A and the actin (24, 29). In addition, as the engagement between the adaptor and the actin flux is modulated by the local protein tyrosine kinase activity (30, 31), FA-mediated viscous drag coefficient can be written as $\zeta_0 \cdot s_1 \cdot \frac{K^2}{K_{0\xi}^2 + K^2}$, where ζ_0 represents the intrinsic lifetime of the bond between ECM-integrin-adaptor and F-actin (32). Therefore, $\xi_0 = \zeta_0 E_0$ (see parameter table S1 and parameter derivations). The Hill coefficient 2 in $\frac{K^2}{K_{0\xi}^2 + K^2}$ reflects the cooperativity in the protein tyrosine kinase activity, *e.g.*, FAK – one of the essential focal adhesion PTK – functions as dimers(33). However, physiologically relevant variations in the Hill coefficient do not cause qualitative changes in the overall model result.

When the actin flux velocity varies over space, it will introduce the deformation of the FA in the lateral direction and, consequently, a shear stress. To derive the relevant formula, let us assume that actin flux velocity only varies in the x-direction. During the time

dt, the two E-I-A molecules at x_1 and x_2 travel with the actin flux over the distances $v_{actin}(x_1,t)\cdot dt$ and $v_{actin}(x_2,t)\cdot dt$, respectively. The change in the lateral distance between these two E-I-A molecules is $\left(v_{actin}(x_1,t)-v_{actin}(x_2,t)\right)\cdot dt$, *i.e.*, causing the deformation of the FA. Now let $x_1 \rightarrow x_2$, the elastic restoring force is $k_{FA}\cdot dx\cdot\frac{\partial v_{actin}}{\partial x}\cdot dt$. Here, k_{FA} is the spring constant of the FA in its lateral direction, which arises from the interaction between the neighboring E-I-As, but is not determined by the tensile elasticity of the E–I–A (s_1) itself. This elastic force should balance with the shear stress $\eta_s\cdot\left(\nabla\cdot\vec{\mathbf{v}}_{actin}\right)\frac{\vec{\mathbf{v}}_{actin}}{\left\|\vec{\mathbf{v}}_{actin}\right\|}\cdot EIA$, where [E–I–A]=1 in this case. Consequently, $\eta_s = k_{FA}\cdot dx\cdot dt$, where dx is the nearest neighboring distance between E–I–A and dt is the same as ζ_0, the lifetime of the bond between E–I–A and the actin flux.

(2.5) Dynamics of stress fiber

The dynamics of SF-mediated contractility and the associated SF elongation are described by the coupled partial differential equations (Eq. (S15)-(S19)), which define a delayed negative feedback. These features are based on well-established experimental observation as elaborated below.

Eqs. (S15) and (S16) describe the PTP-mediated SF formation and the associated actomyosin contraction, respectively. We ignored the detailed dynamics of RhoA activation by PTP and the geometry of SF formation, and only focused on the net mechanical outcome of such signal cascade – the actomyosin contractility exerting upon the FA. It also lumps the overall load-dependence of non-muscle myosin II in its ATPase cycle and the facilitating effect on myosin II ATPase from the SF elongation as well as its intrinsic ECM stiffness-dependence.

$$\frac{\partial M}{\partial t} = \underbrace{k_+^M\cdot\frac{(P/P_0)^{n_{PM}}}{1+(P/P_0)^{n_{PM}}}\cdot(1-M)}_{\text{Actomyosin activation by PTP}} - k_-^M\cdot M\cdot\underbrace{e^{E_{Myo}\cdot\frac{E_0+E}{E_0E}\left\{1+\frac{v_p}{v_0}\right\}-1}}_{\text{Facilitating effect}} \qquad \text{(S15)}$$

$$\vec{F}_{contr} = f_{\max}\cdot M\vec{m} \qquad \text{(S16)}$$

Here, M is the local normalized level of actomyosin contractility at FA, and $\vec{F}_{contr}$ is its effective contractility in the proximal direction along the FA long-axis, defined as the unit vector $\vec{m}$. The $f_{\max}$ is the maximum contractility by actomyosin.

Eq. (S17) captures the experimental observation that the tension at the plus end of F-actin bundle stimulates the formin activity (34, 35).

$$\frac{\partial N}{\partial t} = k_+^N\cdot(1-N)\cdot(e^{\frac{F_{contr}\cdot\delta}{k_BT}}-1) - k_-^N\cdot N \qquad \text{(S17)}$$

N is the activity of the actin nucleation factor for F-actin bundles at the FA that is activated by the contractility, *e.g.*, formins (34, 35) or VASP (36). The force-dependent reaction term in Eq. (S17) is similar to the formula used in the experiments (34, 35), where $\delta = 2.7$ nm is the step size of adding one actin monomer; k_B is the Boltzman constant and T is the temperature. This force-dependence is based on the transition state theory (23, 37), wherein the contraction promote the opening of the formin, thus lowering down the energy barrier of adding actin monomers to the formin-capped plus end of F-actin, analogous to that in (38).

Eq. (S18) describes the dynamics of profilin-actin complex promoted by activated formins. As active formin is a dimer (39, 40), we assume that the Hill coefficient in Eq. (S18) is 2. We note that the essence of model results does not critically hinge on the value of this Hill coefficient. In this picture, the subsequent speed-up of the actin polymerization requires profilin to form a complex with actin monomer that facilitates the actin monomer loading to the plus end of SF (34, 35). Consequently, Eq. (S19) models the SF elongation rate to be proportional to the level of profilin-actin complex.

$$\frac{\partial V}{\partial t} = k_+^V \cdot \frac{N^2}{N_0^2 + N^2} \cdot (1 - V) - k_-^V \cdot V \tag{S18}$$

$$v_p = v_{n0} V \tag{S19}$$

Here, V represents the local level of the profilin-actin complex that binds to the nucleation factor and subsequently delivers the actin monomers to the plus ends of the SF. Therefore, v_p is proportional to the SF elongation rate $v_p = v_{n0} V$, where v_{n0} is the maximum velocity of bundled actin polymerization.

Moreover, experiments show that the characteristic time scale of myosin II contraction is much faster than SF elongation (please see our parameter derivation and table in Section II). Therefore, the above factors (Eqs. (S15)-(S19)) together define a delayed negative feedback.

To appreciate the precise physical picture of concerning the SF elongation and contraction, we further elaborate our mathematical construction of Eqs (S15)-(S19) below. The plus ends of the stress fiber engage with the FA. Stress fiber is a composite structure; its constitutive actomyosin filaments could have relative movement due to the different contractilities. In the context of our model, we attributed the difference in the contractility between different locations within the FA to their underlying FA density differences. Consequently, the contractility per E–I–A remains the same across the proximal half of the FA where the stress fiber impinges upon. It thus follows that, the bundled F-actin polymerization rates promoted by the contractility are uniform across the FA; hence, the stress fibers elongate as one unit. In other words, there is no relative sliding between the F-actin within the stress fiber. The following experimental results support this model assumption. First, the internal viscous drag within the stress fiber arising from the interactions between its constitutive actomyosin filaments is extremely large ($\sim 10^2$ – 10^3 pN·s/nm) (41-43). Second, the force exerted upon individual integrin is ~ 1 – 2 pN in our system, and each ECM-integrin-adaptor complex binds ~ 2 actin filaments (44). The force per actin filament is 0.5 – 1 pN, which can at most drive a filament sliding speed within the

stress fiber of ~ 0.01 – 0.001 nm/s, neglectable compared to the typical stress fiber elongation rate ~ 4 nm/s (45) and ~ 5–10 nm/s elongation rate in our case (see Fig 4B). Therefore, the relative sliding between the actomyosin filaments and the uneven forces within the stress fiber can be ignored.

In addition, VASP is recruited to FA by zyxin (46, 47), which itself is a mechanosensor, i.e., the larger FA traction is, the slower it turns over (48). Thus, the traction force could also promote the activity of VASP at FA, which functions a tetramer (49) and, polymerizes actin filaments by recruiting profilin-actin complexes to the filament plus ends (36), similar to formin. In that case, the Hill coefficient in Eq. (S18) would be 4. Again, we emphasize that the model predictions do not critically depend on this Hill coefficient in Eq. (S18) (data not shown); in the current model, we only consider the case of formin.

Further, the facilitating effects on myosin II ATPase from the stress fiber elongation described by Eq. (S15) can be derived as follows. The ECM-FA-SF module can be treated as a series of connected springs. Upon actomyosin contraction at a very small timescale τ before the effect of load-dependence of myosin II kicks in, the extension of such springs can be written as:

$$\Delta L_{eff} = \Delta L_{ECM} + \Delta L_{SFp} + \Delta L_{FA} \tag{S20}$$

where ΔL_{ECM} is the deformation of ECM, ΔL_{FA} is the deformation of focal adhesion, and ΔL_{SFp} is the elongation of stress fiber due to the actin polymerization. Force balance gives:

$$E \cdot \Delta L_{ECM} = E_0 \cdot \Delta L_{FA} = s_1 \cdot \left(\Delta L_{ECM} + \Delta L_{FA} \right) = E_{eff} \cdot \Delta L_{eff} \tag{S21}$$

where E, E_0 and E_{eff} are the stiffness of ECM, FA and effective stiffness of the ECM-FA-SF system, respectively. Again, $s_1 = \dfrac{E_0 E}{E_0 + E}$ is the effective stiffness of ECM-FA linkage. Taken Eqs. (S20-21) together, we have: $\dfrac{1}{E_{eff}} = \dfrac{E_0 + E}{E_0 E} \cdot \left(1 + \dfrac{\Delta L_{SFp}}{\Delta L_{ECM} + \Delta L_{FA}} \right)$. With $v_0 = \left(\Delta L_{ECM} + \Delta L_{FA} \right) / \tau$ and $v_p = \Delta L_{SFp} / \tau$, we get:

$$E_{eff} = \frac{E_0 E}{E_0 + E} \cdot \frac{1}{\left(1 + v_p / v_0 \right)} \tag{S22}$$

Hereby, $\dfrac{v_p}{v_0}$ represents the ratio between the deformations of ECM-FA linkage and the SF upon the same force during the small timescale τ. v_0 should be intrinsic to the ECM-FA linkage itself and hence a constant independent of v_p. The physical meaning of the Eq. (S22) is: In the "eyes" of the actomyosin contraction, the ECM becomes softer than it really is due to the SF elongation.

As such, the effective deformation of FA is $\Delta L_{eff} = \frac{F}{E_{eff}}$, where F is the actomyosin contractility during the timescale τ. On the other hand, actomyosin contracts by stepping. Therefore, the ECM-FA-SF deformation during τ "expected" by the actomyosin is $\Delta L_{\text{expect}} = \frac{F}{E_{Myo}}$, where E_{Myo} is the effective stiffness inherent to actomyosin and can be estimated from the stalling force and the walking step size (see the parameter derivation). If $\Delta L_{eff} > \Delta L_{\text{expect}}$, the actual deformation is larger than "expected", the actomyosin contraction is "facilitated". According to experiments (50), such facilitating effect compromises the efficiency of myosin II contractility. Hereby we incorporated this facilitating effect into the off rate of actomyosin activity as $k_-^M \sim e^{\frac{\left(\Delta L_{eff} - \Delta L_{\text{expect}}\right)}{\Delta L_{\text{expect}}}}$, which becomes $k_-^M \sim e^{E_{Myo}\cdot\frac{E_0+E}{E_0 E}\left(1+\frac{v_p}{v_0}\right)-1}$ by combining Eqs. (S20-22). It depends on both the SF elongation rate and the ECM stiffness. As we discussed below, it correctly predicted the linear dependence of FA traction on ECM stiffness evidenced in experiments (51, 52), which thus in part validates the above theoretical deduction of the facilitating effects.

(2.6) Total traction force

The total FA traction is thus $\vec{F}_{adh} + \vec{F}_{contr}$ that naturally introduces two distinct force distributions within the FA.

II. Model Parameters

1. Parameter tables

Table S1 Parameters in mechanics

Parameter Symbol	Parameter description	Measured values	Value used in the model	Reference
κ_m	Membrane bending modulus	4.2×10^{-19} J	4.2×10^{-19} J	(53, 54)
σ_m	Membrane surface tension	10^{-4} – 10^{-5} J/m^2	10^{-4} J/m^2	(53, 54)
λ_m	Membrane viscous drag coefficient	2×10^9 Pa·s/m	2×10^9 Pa·s/m	(55)
ξ_0	Viscous drag coefficient between actin flux and FA	17.5–1050 kPa·s/μm	150 kPa·s/μm	(1, 32, 44, 56-58)
η	Dynamic viscosity of actin flux	10 kPa·s/μm	10 kPa·s/μm	(55)
α_A	Adaptor drift coefficient with actin flux	0.4–0.8	0.5	(8, 59)
α_{IA}	IA drift coefficient with actin flux	0.1–0.4	0.1	(8, 59)
η_s	Shear stress coefficient	25–300 kPa·s	100 kPa·s	(32, 58, 60)
ρ_0	Bulk density of F-actin	~40 kg/m^3	~40 kg/m^3	(61)
k_p	Total actin polymerization rate	5~50 nm/s	25 nm/s	(8, 62)
$\bar{k}$	The effective resistance constant to the membrane protrusion from the rest of the cell membrane	~1kPa/μm	1kPa/μm	(4, 53, 54)

Table S2 Parameters in chemical reactions

Parameter Symbol	Parameter description	Measured values	Value used in the model	Reference
D	Diffusion constant for unanchored FA components	10^{-5}–10^{-6} μm²/s	10^{-5} μm²/s	(59, 63)
$k_{\rho}^{(0)}$	Maximum actin depolymerization rate constant near LP/LM interface	0.015–0.03/s	0.02/s	(17, 64)
k_{-}^{I}	The off rate constant of free integrin (I) into cytoplasm	0.008–0.013 /s	0.01 /s	(65)
k_{-}^{A}	The off rate constant of free adaptor (A) into cytoplasm	0.008~0.013 /s	0.01/s	(65)
$k_{r_E}^{I}$	The rate constant of integrin (I) recruitment by ECM (E)	0.01–1 /s	0.06 /s	(1, 31, 48, 65-68)
$k_{r_A}^{I}$	The rate constant of integrin (I) recruitment by adaptor (A)	0.01–1 /s	0.06 /s	(1, 31, 48, 65-68)
$k_{r_I}^{A}$	The rate constant of adaptor recruitment by I and IE	0.01–1 /s	0.04/s	(1, 31, 48, 65-68)
k_{+}^{IA}	The rate constant of conversion from I and A to IA	0.01–1 /s	0.08/s	(1, 31, 48, 65-68)
$k_{+}^{(1)}$	The intrinsic rate constant of conversion from IA to EIA	0.01–1 /s	0.015/s	(1, 31, 48, 65-68)
k_{-}^{IA}	The rate constant of conversion from IA to I and A	0.01–1 /s	0.5 /s	(1, 31, 48, 65-68)
$k_{-}^{(1)}$	The intrinsic rate constant of conversion from EIA to IA	0.01–1 /s	0.1/s	(1, 31, 48, 65-68)
k_{-}^{EI}	The rate constant of conversion from EI to I and E	0.01–1 /s	0.6/s	(1, 31, 48, 63, 65-68)
k_{+}^{EI}	The rate constant of conversion from I to EI	0.01–1 /s	0.05 /s	(1, 31, 48, 65-68)
$k_{-}^{(0)}$	The intrinsic rate constant of conversion from EIA to EI	0.01–1 /s	0.05/s	(1, 31, 48, 65-68)
$k_{+}^{(0)}$	The intrinsic rate constant of conversion from EI and A to EIA	0.01–1 /s	0.015/s	(1, 31, 48, 65-68)
$k_{+F}^{(0)}$	Maximum rate constant of force dependent EI to EIA conversion	0.75–5 /s	5/s	(6, 7, 21, 69)
$k_{+F}^{(1)}$	Maximum rate constant of force dependent IA to EIA conversion	0.75–5 /s	2.5/s	(6, 7, 21, 69)
F_0	The threshold stress above which adaptors exhibit catch bond behavior	< 2 kPa	1.2 kPa	(6, 7, 21, 69)
n_0	Hill coefficient for adaptor-mediated catch bond behavior	>1	2	(6, 7, 21)
k_{+}^{K}	The activation rate constant of PTK	>0.1/s	0.2/s	(31, 48, 65-68)
k_{-}^{K}	The de-activation rate constant of PTK	0.1–0.2 /s	0.1/s	(31, 68)
F_{MK}	The threshold stress above which PTK exhibits catch bond behaviors	<1 kPa	0.6 kPa	(70-73)
β_p	The threshold PTP activity above which it inhibits PTK	0–1	0.15	(25)
n_p	Hill coefficient of PTK inhibition by PTP	>1	2	(25)
k_{+}^{P}	The activation rate constant of PTP		0.1/s	Model based
k_{-}^{P}	The de-activation rate constant of PTP		0.05/s	Model based
β_K	The threshold activity above which PTK inhibits PTP	0–1	0.35	(25)
n_K	Hill coefficient of PTP inhibition by PTK	>1	2	(25)
E_0	The effective stiffness of FA complex	3.5–70 kPa	10 kPa	(1, 44, 56-58)
$K_{0\xi}$	The threshold PTK activity above which it reinforces the FA-actin flux engagement	0–1	0.15	(30, 31)
k_{+}^{M}	The activation rate constant of actomyosin by PTP	2–9/s	5/s	(74)
P_0	The threshold activity above which PTP activates actomyosin		0.55	Model based
n_{PM}	The Hill coefficient of the actomyosin activation by PTP		3	Model based
k_{-}^{M}	The de-activation rate constant of actomyosin contractility	0.25–0.5 /s	0.3/s	(50, 75)
E_{myo}	The intrinsic stiffness of actomyosin	6–100 kPa	12 kPa	(43, 58, 75, 76)

v_0	The characteristic velocity of FA-ECM complex deformation upon actomyosin contraction	5–20 nm/s	15 nm/s	(50-52, 77)
v_{n0}	The maximum SF elongation rate	20–200 nm/s	45 nm/s	(34, 35, 78-80)
k_+^V	The binding rate constant of profilin-actin complex to the SF-localized actin nucleation factor	0.1–1 /s	0.3/s	(31, 48, 65-68)
k_-^V	The disassociation rate constant of profilin-actin complex from SF-localized actin nucleation factor	0.1–1 /s	0.3/s	(31, 48, 65-68)
N_0	The threshold SF-localized actin nucleation factor level above which it promotes the SF elongation	0–1	0.13	(34, 35)
k_+^N	The activation rate constant of SF-localized actin nucleation factor	0.1–1 /s	0.25/s	(31, 48, 65-68)
k_-^N	The de-activation rate constant of SF-localized actin nucleation factor	0.1–1/s	0.125/s	(31, 48, 65-68)
f_{max}	Maximum contractility stress by actomyosin	1–9 kPa	8 kPa	(1, 73, 76, 81)

2. Parameter derivations/considerations

This section summarizes the model parameter estimation based on the experimental observations. As we simplified the model as 2-D problem, we re-scaled any 3-D mechanical parameters by the thickness of the LP (200 nm) to fit the needs of our simulation. The concentrations of FA components are normalized by the maximum occupancy, which corresponds to the density of integrin in FA measured as ~ 1000/μm^2 (58). Most of the model parameters vary across the range within one-order-of-magnitude. We did phase diagram calculations for sensitivity test, in according to these parameter variations. We found that the model results remain qualitatively robust against these variations (as demonstrated by the supplemental figures).

Diffusion constants for FA components *D:*

Rossier et al. measured the diffusion constant of integrin and an adaptor protein talin inside and outside of the FA (59) and showed that the integrins inside the FA domain are mainly immobilized. They also measured the rearward speed of integrins and adaptors ~ 2 nm/s, which represents the drifting velocity of the unanchored integrins and adaptors "hovering overhead" the FA. That means the drift due to the diffusion *D* of these proteins must be less than 2nm/s, i.e., $v\Delta t > 2\sqrt{D\Delta t}$ if we assume two dimensions; otherwise, one will observe the random instead of directional drifting velocity. Consequently, $D < v^2\Delta t / 4$, where Δt is the time it takes for the free integrin to fully anchor to ECM. Experiments showed that the binding time for integrins to fibronectin Δt~ 0.6 – 6 sec (63). This gives rise to the upper limit of the diffusion for free integrin in the range of 10^{-5} – 10^{-6} μm^2/s. We expect the diffusion of the free adaptors in the similar range as that of integrin. We thus use the same 10^{-5} μm^2/s for free integrin, adaptor, integrin-adaptor complex and for that of PTK and PTP activities in the model, because the model results remain essentially the same when the diffusion constant varies from 10^{-3} to 10^{-6} μm^2/s (data not shown). Of further note, due to the small diffusion, the drifting becomes more prominent. As such, an oblong shape of the FA emerges from the competition between the small diffusions and the drifting.

Actin depolymerization rate constant at LP/LM boundary $k_\rho^{(0)}$:

In the context of FA and actin retrograde flux, experiments show that most of F-actin is depolymerized at the LP/LM boundary (17). Since the turnover cycle of the actin in cells is about 30 – 60 s (17, 64), it suggests that $k_{\rho}^{(0)}$ is ~ 0.015 – 0.03 /s. We use 0.02/s in the model.

Chemical reaction rates of FA components:

Because the model is built on the functional module level in accordance to the four-layered structure of FA (1), each of these modules could include multiple molecular species. For instance, the adaptor module in the model includes talin, paxillin, zyxin, α-actinin, and vinculin. Consequently, the reaction rates used in the model reflect the overall dynamics of the ensemble of these proteins for each of the functional modules. In this regard, experiments have made extensive efforts in measuring the overall assembly and disassembly rates of FA (31, 48, 65-68). For different proteins within the same functional module, experiments yield slightly different on and off rates at the FA, thus providing the range of the corresponding model parameter values. We thus drew supports from these well-established results in deducing the relevant chemical reaction rates among E-I-A, E-I, I-A, I, and A (see the model parameter table S2 for details).

Catch bond behavior of FA components:

Experiments show that both integrins and the FA adaptors can behave like catch bonds under tension (6, 21). For instance, single molecule stretching experiment demonstrated that a 2 pN force can extend single talin and expose more binding sites for recruitments of vinculin (another FA adaptor). The experimental data obtained by using either living cells or self-assembled actomyosin complexes confirmed that talin is stretched in FA and behaves as a catch bond (7, 69, 82). While the exposures of the more binding sites in talin upon stretching are discrete events and highly non-linear (6), the model is concerned with the continuum. We therefore interpolated such observed discrete events in the model and map them into continuous Michaelis-Menten kinetics equations for recruitment of A and I-A: $k_{+F}^{(0)} \frac{\left(F_{EIA}/F_0\right)^{n_0}}{1+\left(F_{EIA}/F_0\right)^{n_0}}$ and $k_{+F}^{(1)} \frac{\left(F_{EIA}/F_0\right)^{n_0}}{1+\left(F_{EIA}/F_0\right)^{n_0}}$, where F_{EIA} is the force on fully anchored E-I-A. Consequently, the threshold force F_0 that invokes the more adaptor recruitment must be < 2 pN, and the Hill coefficient n_0 must be >1. We used F_0=1.2 pN, and n_0 = 2 in the model, the variation of which in the physiological range will not affect the qualitative model conclusion.

Note that, while β1 integrin also exhibit catch bond behaviors upon tension (21), the threshold force to activate such molecular clutch is ~ 20 pN (21), which is much larger than the 1-3 pN per integrin involved here. The model therefore neglected the contribution of integrin in catch bonds.

Next, we can calculate the parameter range of $k_{+F}^{(0)}$ and $k_{+F}^{(1)}$. The unfolding rate of talin is at 2/s for zero force and increases to 5/s at the force of 20 pN (Fig 4F of Ref.(6)). The unfolding of talin will expose ~5-7 binding sites for further vinculin recruitment (6, 7). Consequently, the increase on the E-I-A assembly rate is ~(3/s)*(5–7)/20pN= (0.75–1)/(s·pN). Given that the typical traction force on I-E-A is around 1~5 pN, the overall rate

for the force dependent conversion from E-I to E-I-A ($k_{+F}^{(0)} \frac{\left(F_{EIA}/F_0\right)^{n_0}}{1+\left(F_{EIA}/F_0\right)^{n_0}}$) and I-A to E-I-A ($k_{+F}^{(1)} \frac{\left(F_{EIA}/F_0\right)^{n_0}}{1+\left(F_{EIA}/F_0\right)^{n_0}}$) would be in the order of ~0.75-5/s. In the model, we used $k_{+F}^{(0)}$~ 5/s and $k_{+F}^{(1)}$~ 2.5/s for the maximum increase in the force-dependent E-I-A assembly rate.

The effective resistance constant to the membrane protrusion from the rest of cell membrane $\bar{k}$:

When actin polymerization pushes on the plasma membrane protruding it forward, it is resisted by the other part of the membrane, mainly from those flanking the leading edge. The membrane area change upon protrusion is $\Delta A = 2 \cdot h \cdot d_{width}$, where h is the protruding distance and d_{width} = 2.3 μm is the width of the simulation box. As thus, the membrane energy stored is $W = \sigma_m \Delta A$ and $\sigma_m \sim 10^{-4} J/m^2$ is the membrane surface tension (53, 54). The average membrane resistance force therefore is $W/h = 2\sigma_m d_{width} = 4.6 \times 10^{-10} N = 460 pN$. The protruding area is the height of the LP (200 nm) multiplied by the width of the simulation box (2.3 μm). Therefore, the corresponding resistance stress f_e is in the range of kPa. Typical in vivo protrusion of the LP is in the range a few microns before retraction(4). This provides an estimate of $\bar{k}$ in the order of 1 kPa/μm, which is the nominal value chosen in our simulation. Varying $\bar{k}$ will only reflect how easily the membrane can be protruded and reciprocally the actin retrograde flux, and will not affect the qualitative model result (data not shown).

Catch bond behavior of PTK activity F_{MK}:

Experiments show that PTK activity is force dependent both in vitro and in vivo (70, 71). It is known that FA traction stress is ~1-5 kPa across the physiological range of ECM stiffness (72, 73). Even for the very soft ECM in which the FA traction is ~ 1 kPa, PTK is known to get activated (70, 71). Thus, the threshold traction stress for activating PTK (F_{MK}) should be < 1 kPa. In the model, we chose F_{MK} ~ 0.6 kPa in the model, corresponding to ~ 0.6 pN per E-I-A linkage.

The effective stiffness of FA complex E_0:

The spring constant of integrin-mediated adhesion is measured to be 0.2 – 0.4 pN/nm along its vertical direction (56). This value corresponds to the tensile elasticity of the E-I-A complex. Because the above experiment used collagen type I fibrils of 67 nm in thickness and 3 nm in height to cover glass-slip as the ECM, the effective stiffness of the ECM experienced by individual integrin dimers is extremely large (~ GPa) (57). Consider the E-I-A as a series of connected springs, the measured spring constant essentially reflects the elasticity of I-A. To convert to the Young's modulus of the FA complex (the stiffness E_0 in the model), the spring constant needs to be multiplied by the FA height divided by the cross section area of FA. By iPALM it was shown that height of integrin and FA adaptor protein layers can be ~ 70 – 90 nm (1). In addition, Patla et al.(44) measured the mean distance between the neighboring centers of mass of FA clusters (E-I-A) as 43 ± 20 nm, consistent with the ~ 33 nm derived from the average integrin density in FA (58). This

means the average filling area of each FA cluster is ~ 500 – 4000 nm^2. We can then estimate the effective stiffness of FA complex E_0 ~ 3.5 – 70 kPa. We typically used 10 kPa in the model.

The viscous drag coefficient between actin flux and FA ξ_0:

It is given by $\xi = \frac{\zeta_0 \cdot E_0 \cdot E}{E_0 + E} = \frac{\xi_0 \cdot E}{E_0 + E}$, where $\xi_0 = \zeta_0 \cdot E_0$. Here, $\zeta_0$is the lifetime of the adaptor-actin, which is ~1 – 3 sec (32). Since E_0 is ~ 3.5 –70 kPa (see the above), ξ_0 is ~ 17.5 – 1050 kPa·s/μm, after taking into account of the thickness of the LP ~ 200 nm. In the simulation, we typically used ξ_0=150 kPa·s/μm.

Shear stress coefficient η_s:

We estimated the shear stress coefficient $\eta_s = k_{FA} \cdot dy \cdot dt$. In reality, *dy* is the nearest neighboring distance between E-I-A is defined by the integrin density in FA (~1000/μm^2) (58), which leads to *dy* ~ 33 nm. And *dt* is the lifetime of the bond between E-I-A and the actin flux, which is ~ 1-3 sec (32). Taken together, the shear stress coefficient is 25 – 300 pN·s (32, 60), which become 25 – 300 kPa·s, after scaled with the density of integrin in the FA (1000/μm^2). We used η_s=100 kPa·s in the model.

Intrinsic stiffness arising from actomyosin contraction upon bundled F-actin E_{Myo}:

The stall force for the non-muscle stress fiber is ~ 100pN (76). Given the average NMM II step size is about ~10 nm (75), the effective stiffness of actomyosin is ~ 10 pN/nm. Given that its typical length of stress fiber contractile unit is ~ 1μm, and each stress fiber has the cross section area ~ (100nm)^2 – (200nm)^2 (76), the effective stiffness of stress fibers is thus ~ 250 – 1000 kPa. Because the integrin density in FA is ~ 1000/μm^2 (58) , each stress fiber will thus cover ~ 10 – 40 integrins. As such, the effective stiffness of the actomyosin felt by each integrin will be reduced by ~ 10 – 40 folds. The estimated intrinsic stiffness of actomyosin contraction E_{Myo} is thus ~ 6 – 100 kPa. Alternatively, the tensile stiffness of a single muscle stress fiber is measured to be ~ 1500 kPa (43). Since it has a diameter ~ 200 nm, this stiffness corresponds to 37.5 kPa following the above derivation procedure. As muscle stress fiber is expected to be stronger than its non-muscle cousin, the real intrinsic stiffness of the non-muscle stress fiber in our case should be near the lower end of the 6 – 100 kPa ranges. We thus used E_{myo}= 12 kPa in the model.

Characteristic velocity of FA-ECM complex deformation during contraction v_0:

The deformation of ECM is ~130 nm independent of ECM stiffness (51, 52), while it can be ~ 100nm for talin (1, 7) and ~ 10nm for integrin (83). Together, the total length of extension can ~ 100 –200nm. Given the typical of the non-muscle myosin II ATPase cycle in stress fiber is around 10~20 seconds (50, 77). v_0 is thus ~5–20 nm/s. The typical value of v_0 is 15 nm/s in the model.

Maximum traction stress by actomyosin on FA f_{max}:

Each stress fiber with a cross section of 0.01 – 0.04 μm^2 can exert ~ 100 pN force(76), which produces ~ 2.5 – 10 kPa traction stress. As demonstrated in iPALM experiments(1), the distance between adaptor talin C- and N-terminals in z-direction is ~ 19 – 48 nm. Given that talin is ~ 60 nm long (81), it means that the FA adaptor binds the stress fiber with a tilt angle ~ 20 – 50 degrees. Thus, the traction stress in the lateral direction of the FA is ~ 1 – 9 kPa. The typical maximum traction stress chosen in the model is 8 kPa, comparable with the measured 5.5 kPa FA traction stress (73).

III. Additional Model Phase Diagram Studies – The necessity of model ingredients

The model includes the components essential for FA growth and integrates them into intricate regulatory biochemical feedbacks that react upon and, reciprocally, govern over the mechanical forces (Fig 1). We endeavored to simplify the model without losing the biological essence. In the main text, we illustrated the overall outcome when these basic ingredients work together properly (Figs 2 and 3), along with the phenotypes arising from perturbations stress fiber dynamics (Figs 4-6).

The experiments developed to validate the model and to dissect the mechanistic basis of traction force oscillations within a FA demonstrate only a part of model capacity. While one might in principle build a simpler model that could account for FA traction oscillation equally well, we aimed to provide the coherent depiction of FA growth. This comprehensive model reveals itself in dissecting and explaining the contributions of the individual FA components in such whole process, resolving contradictory experiment observations, and addressing a number of basic questions in FA formation, maturation, and mechanosensing.

As shown below (Fig S2-S4, S6-S7, S10), the model parameter sensitivity investigation by phase diagram calculations not only attests to the model robustness, but also demonstrates that missing any one of these ingredients in the model will result in the corresponding phenotypes, some of which are evidenced in experiments. This way, we provided the model rationale of integrating these FA components, and its full predictive capacity.

Distal traction peak requires Arp2/3-mediated actin flux

Our model predicted that the magnitude of the distal traction peak stemmed from the engagement between the FA and the local actin flux. For any FA with traction peak position oscillation (as in Figs 2C and 2D), the model further predicted that reducing the actin flux or weakening the FA-actin flux engagement decreased the magnitude of the distal peak, and constrained the FA traction maximum to the FA center (Fig S6A).

To test this predicted role of actin flux in FA traction generation, we performed two sets of experiments. First, we harnessed a well-established phenomenon in control cells; specifically, there is a decreasing gradient of actin flux from the LP toward the LM (64). As described previously (72), we analyzed the population distribution of traction forces in FAs located either at the LP/LM interface, which experience a steep gradient of actin flux, and FAs located deep inside the LM with vanishing actin flux (Fig S6B). We noted that there

could be different types of adhesion sites in cells that are fundamentally different from the FAs we aimed to analyze. For instance, fibrillar adhesions that participate in ECM remodeling locate toward the cell center, but exert minimal traction force (84). To make sure that only FAs were chosen for the analysis, we stained the cells with tensin antibody (a well-established marker of fibrillar adhesions). We found that both peripheral adhesions and those located deep inside the LM were negative for tensin, but contained all molecular markers of FAs (paxillin, vinculin, talin, and FAK) (Figs S7A-F). These results suggested that the observed difference in FA traction force profile between the FAs near the cell edge and those inside the cell body could not be attributed to fundamentally different types of adhesions; instead, it was likely caused by the spatial variation of actin flow. Our measurements were fully consistent with the predicted correlation between the traction force profiles within the FAs and the FA position relative to the cell leading edge. The further away an FA was from the cell leading edge, the less it exhibited a distal traction peak, and the more it exhibited only the central traction peak (the columns (a-b) in Fig S6C).

Second, to further explore the origin of the distal traction peak, we directly perturbed actin flux. We used a pharmacological agent (CK-666) to inhibit Arp2/3 complexes that in turn attenuated branching actin polymerization and actin retrograde flux (85, 86). We treated cells with 100 μM CK-666 for 4-6 hours. This treatment suppressed LP formation as indicated by the disappearance of cortactin from the cell periphery (Fig S7B) and by the significant decrease in the actin retrograde flux rate near the cell edge (~33%, $p < 10^{-5}$, Fig S6B(i-ii)). According to the model, this decrease in actin retrograde flux rate dramatically reduced the distal traction peaks of the FAs that were located at the cell periphery and, consequently, shifted the traction maximum toward the centers of these individual FAs (Fig S6A). Indeed, our TFM measurements showed that the distal peak in the FAs near the cell edge disappeared upon Arp2/3 inhibition (compare columns (a) and (c) in Fig S6C). In addition, FAs located deep inside the cell body displayed only the central traction peak in control cells (column (b) in Fig S6C) and remained so in CK-666 treated cells (column (d) in Fig S6C). We cautioned that, however, the CK666 treatment might fundamentally alter the FA formation mechanism, which would make it difficult to interpret our experimental data. We therefore repeated TFM experiments using cells with acute CK-666 treatment (20 min). This acute treatment was sufficient to suppress LP formation as confirmed by cortactin immunostaining (Fig S7B), and it also shifted traction peak position within each FA in the cell edge from the FA distal end (as in control) to the FA center (column (e) in Fig S6C). Meanwhile, the traction peak position within the FAs inside the cell body remained insensitive to this acute drug treatment (column (f) in Fig S6C). This finding confirmed our previous results by the prolong drug treatment (4 hours), and further suggested that retrograde actin flow contributed to the distal traction peak, while it may not govern the central traction peak. To further confirm this conclusion, we immunostained the cells with both acute and prolong CK-666 treatment. Our data demonstrated that the drug treatments only had a minor (if any) effect on molecular composition of FAs (Figs S7C-F). Specifically, for the cells treated with CK-666 for up to 4hr, we did not detect significant difference in distribution of any tested FA marker as compared with control (paxillin, vinculin, talin, FAK, and FAK phosphorylated on Thy397). Together, our experimental findings thus supported that the distal traction peak arose from Arp2/3-mediated actin flux, and that the central traction peak stemmed from an Arp2/3-independent source.

Effects of FA-actin flux engagement on FA growth and traction

The model predicts that actin retrograde flux engages with the nascent FA upon first contact, from which arise the viscous drag and the shear stress. These mechanical forces will pull the FA that at first strengthen the E–I–A linkage (catch-bond behavior), and ultimately break it (slip-bond behavior), promoting the drifting. It is the re-binding to the ECM of these disengaged drifting FA components that confer the elongated FA growth downstream of the actin flux, resulting in the oblong shape of the maturing FAs.

According this model, the FA mechanical engagement with the actin flux thus pave the way for the FA maturation. The phase diagram of Fig S2A shows that proper FA growth hinges on the actin flux velocity and its engagement with FA. The nascent FA can never grow, when the actin flux is too small, too large, or its engagement with FA is too weak (Fig S2B). This is because, the strengthening of the E–I–A linkage cannot be sufficiently promoted under these conditions. Consequently, the FA traction force remains too low to break the E–I–A linkage and promote the drifting, and hence no FA growth. Conversely, when the actin flux is too large, so is the stretch upon the FA, which drives the breakage, instead the strengthening, of the E–I–A linkage. In addition, as the actin flux is too fast, these drifting FA components don't have enough dwell time to anchor to ECM before drifting again. In the end, the level of fully anchored E–I–A remains low and so does the FA traction force (Fig S2C). This model result thus recapitulates the observed dependence of FA traction force on the actin flux velocity (62, 87).

On the other hand, at intermediate velocity of the actin flux, if the actin flux engagement with FA is too strong, nascent FAs can only have limited growth (less than 2 μm in length) and never evolve into the matured ones (longer than 4 μm) (Fig S2B). This is because a stronger FA-actin flux engagement leads to a higher PTK activity within the FA, which in turn, inhibits PTP activity and might suppress stress fiber contractility (Fig S2D). Without stabilization by stress fiber, the maximum growth of the nascent FA in this case will be eventually limited by the actin depolymerization at the LP/LM interface (17), which is only ~ 2-3 μm away from the cell leading edge.

Only when both actin flux and its engagement with FA are at appropriately sufficient levels, the nascent FA can mature (Figs S2A and S2B). Thus, before the inauguration of stress fiber engagement, the traction force profile exhibits a significant decreasing gradient from the distal to the proximal tip of the FA (the orange line in the (i) of Fig S2E), which provides the sufficiently disparate mechanical environment within the FA that tips the PTK-PTP antagonism toward PTP pathway. This toggle switch promotes the FA-stress fiber engagement. When stress fiber contracts upon the FA, it further strengthens the local E-I-A linkage via catch bonds, converting more of the drifting I-A and A into the fully anchored E-I-A in the newly acquired proximal half of the FA area (the orange lines in (ii)-(iii) of Fig S3E). Thus, the stress fiber contraction promotes the FA growth and stabilization. This model insight is consistent with the observations that actin flux promotes elongated FA growth near the cell leading edge (65), and that actomyosin contractility is necessary for FA maturation (88). The spatiotemporal evolution of the distinct mechanochemical properties of the FA across its long-axis is in line with their different disassembly modes evidenced in experiments (89-91), and the observed developments of the local FA protein profile as the FA matures from its nascent stage (92).

Interestingly, the model predicts two distinct behaviors of traction oscillations within the normal zone of FA maturation (Fig S2A). When the FA-actin flux engagement is relative low, the distal traction peak herein is even lower than the minimum of the central

traction peak during its oscillation. Therefore, the FA traction peak always resides near the FA center, and only its peak magnitude oscillates. Only when the distal traction peak mediated by the FA-actin flux interaction is higher than the minimum of the central traction peak, do both the position and the magnitude of the FA traction peak oscillate, as evidenced by our experiments.

Effects of actin flux-mediated viscous drag and shear stress on FA dynamics

Figs S2A-E suggest that FA-localized spatial distribution of traction force underlies the toggle switch from PTK- to PTP-mediated pathway localized in the FA and thus regulates the dynamics of FAs. Such traction force at the early stage of FA stems from the FA-actin flux interaction and consists of the viscous drag and the shear stress that arise from the relative velocity between the actin flux and the FA, and the spatial gradient in actin flux velocity along the FA, respectively. However, individual contributions of these distinct mechanical interactions to the overall profile of traction force and in activation of PTK-PTP toggle switch remains unknown.

Without viscous drag, our model suggests that the nascent FA cannot establish sufficient mechanical engagement with the actin flux at the first place (Fig S2F). As such, the nascent FA won't be sizable actin flux gradient and consequently, no shear stress is invoked neither. Ultimately, the nascent FA won't grow at all. On the other hand, turning off the shear stress in the model significantly reduces the distal traction peak (the blue lines in Fig S2E), the resulting profile of which is in stark contrast to that evidenced in the control experiments (Fig 2 in the main text). However, the decreasing traction force gradient mediated by the FA-actin flux interaction still persists in this scenario, which is underpinned by more drifting and less fully anchored FA components within the FA toward the proximal end (the blue lines in Fig S2E). Consequently, PTP and the stress fiber contractility can still get activated in the newly formed FA area, promoting the FA maturation. Note that, shear stress stems from the FA linkage deformation upon interacting with actin flux, e.g., talin extends upon stretching (6). Our model results suggest that while it is necessary to account for the observed FA traction force profile (Fig 2 in the main text), the shear stress itself might not be essential for FA maturation. Instead, it might be just reminiscent of an intrinsic aspect of the catch bond nature for FA adaptor proteins.

Effects of the catch-slip bonds on FA dynamics

Because the drifting of FA components (A and I–A) introduces the weaker interaction with actin than their fully anchored counterpart (E–I–A), it results in the decreasing gradient of actin flux-mediated traction force from the distal end. It is such decreasing gradient that tips the balance toward to PTP activation near the FA proximal end, stress fiber engagement, and FA maturation. Since the drifting is the balanced act arising from the catch and the slip bond behaviors, we next examined to what extent catch and slip bonds affect the FA dynamics.

Fig S2G shows that without catch bond the E–I–A complex cannot be strengthened upon stretching and breaks apart into drifting components (A and I–A) by an actin flux. Although PTK activity is low in this case, PTP is also low due to the lower density of FA components (E–I–A and I–A) (Fig S2G). The end result is, the nascent FA interacts with the actin flux weakly, cannot mature, and eventually disappears. On the other hand, without slip bonds the distal traction peak builds up and concentration of drifting components (A and I–

A) decreases (Fig S2H). As mechanical tension on FA increases, it also increases PTK activity to unusually high level and inhibits the PTP. Consequently, the stress fiber cannot impinge upon the FA, neither can the nascent FA grow. In both cases, the mechanosensing of FA on ECM stiffness is greatly compromised due to the loss of stress fiber-mediated actomyosin contractility (Fig S2I). Therefore, the model predicts that proper FA maturation entails both the catch bond and the slip bond behaviors of the FA, which is consistent with their essential roles indicated by experiments (6, 8, 65, 93-96).

Effects of the antagonism between PTK and PTP on FA dynamics

Next we used computational modeling to determine spatiotemporal pattern of PTK/PTP activity in a FA and to uncover how this pattern regulates FA mechanosensing. As shown in Fig S3, proper PTK activation by an actin flux is critical for FA maturation and for transition from the actin flux-mediated to stress fiber-mediated FA engagement within the same maturing FA. Fig 2B shows a typical example of the spatio-temporal evolution of FA-localized PTK activity: It first concentrates throughout the nascent FA, then begin to spread in parallel with the FA centripetal growth. As mechanosensitive PTKs get activated by an actin flux, it further potentiates the FA-actin flux engagement and forms a positive feedback loop. Culmination of this feedback loop leads to a decreasing gradient in the PTK activity, mirroring that of the traction force before the stress fiber-mediated contractility kicks in. Thus, spatial gradient in PTK activity tips the balance toward the PTP activation in the proximal half of the growing FA, the stress fiber engagement, and further FA maturation.

Clearly, PTK activity holds the key for such dynamic transition. Along this line, the model predicts that nascent FA cannot grow upon inhibition of PTK activity (Fig S3A), because it now cannot establish strong engagement with the actin flux. Without sufficient traction force, the catch bond-mediated positive feedback cannot be invoked to strengthen the E–I–A linkage. And hence, the nascent FA will eventually be washed away by the actin flux once the bonds in E–I–A break apart. Interestingly, the model further predicts that PTK inhibition does not affect the FA once it matures (Fig S3B). This is because inhibition of PTK will reciprocally further activate the local PTP, which locally elicits the stress fiber-mediated contractility. As long as enough traction force remains, the FA will be stabilized, even if its engagement with the actin flux is abrogated. In fact, PTK is known to phosphorylate the myosin light chain kinase and inactivate myosin II (89). If we take this observation into account, our model would predict that PTK inhibition will compromise the turnover of the matured FA. On the other hand, when PTK is over-activated, our calculation suggests that nascent FA cannot mature into large FA (Fig S3C), because the PTP now get completely inhibited. Hence, no stress fiber-mediated contractility could impinge upon and further stabilize the FA, once the FA growth passes the LP/LM interface where the actin flux gets depolymerized. As such, the FA can only have limited growth. Moreover, for matured FA in which the PTP is activated at its proximal half, the moderate PTK over-activation cannot shift the balance back to the PTK domination due to the bistable nature of the PTK/PTP antagonism (Fig S3D). Of course, if the PTK gets over-activated even higher, it will eventually inhibit PTP and the stress fiber contractility, which will cause the disassembly of the proximal half of the FA (Fig S3D). This disparate response from the FA at different stages could explain the seemingly contradictory observations that FAK – one of the major PTKs is essential for both the assembly and the disassembly of FA (31, 89, 97-103).

We also explored the effects of the PTK/PTP antagonism on traction peak oscillations. Figs S3E and S3F are the calculated phase diagrams on how the traction

oscillation depends on the characteristics of the PTK/PTP toggle switch. They show that the traction oscillation is a general feature that can be robustly realized across a broad range of the model parameters.

Effects of SF elongation and ECM stiffness on actomyosin II contractility and FA dynamics

Not only is the actomyosin contractility essential for FA maturation, but also does its negative feedback with the SF elongation dictate the center traction peak oscillation and the efficient mechanosensing of over a broader ECM stiffness range (Fig 6 in the main text). In this section, we will explore how the traction oscillatory behavior depends on the factors pertaining to actomyosin contractility and SF elongation. The phase diagram studies in Figs S4A and S4B show that the FA traction oscillation is a general feature of the stress fiber-mediated negative feedback, which can be realized in the broad range of the model parameter space. As long as the actomyosin contractility and the stress fiber elongation are at off paces, the central traction peak always oscillates.

Fig S4C provides a typical example on the evolution of the FA traction peak magnitude and position oscillation over time, corresponding to the nominal case in the model. Herein, the magnitude and the position are clearly in anti-phase, quantitatively consistent with the experiment observations (72). In comparison, when the actomyosin contractility is inhibited, the FA traction oscillation over time and space is diminished (Fig S4D). Notably, the FA in this case still grows centripetally due to the actin flux-mediated drifting (Fig S4E). However, the center traction peak disappears while the actin flux-mediated distal traction peak persists.

What lies at the core of the stress fiber-mediated negative feedback is the facilitating effect on the actomyosin contractility, whose dependence on ECM stiffness and the stress fiber elongation is theoretically derived in this model. We found that the FA traction scales linearly with ECM stiffness over a broad range (Fig 6). The traction stress changes from about 1 kPa to 2.2 kPa when the ECM stiffness changes from 4 kPa to 30 kPa. To compare the results with the experiments on micropillar (51, 52), we converted the traction stress to traction force following their scheme (51, 52): the micropillar has the radius of ~1 μm, the traction force can be calculated by $F_{force} = F_{stress} \cdot A$, where A is the area of a single pillar. Therefore the corresponding traction force change of 1.2 kPa is ~3.7 nN in the micropillar experiments. Based on the conversion from experimental setup using $k = 4\pi aE/9$ (51, 52), the corresponding spring constants of the micropillars for ECM stiffness of 4 kPa and 30 kPa are 5.5 and 42 nN/μm. Here, a is the radius of the pillars (~ 1 μm), E is the ECM stiffness, and k is the spring constant of a micropillar. As such, the slope of our FA traction vs. ECM elastic constant curve yields a constant length ~ 100 nm, which quantitatively accounts for the observation that cells typically stretch ECM to the same distance and gauges the needed traction force in cell migration (51, 52). The agreement with the experimental observation thus lends support to our derived formula on the facilitating effect on actomyosin contractility.

IV. Supplemental Figures

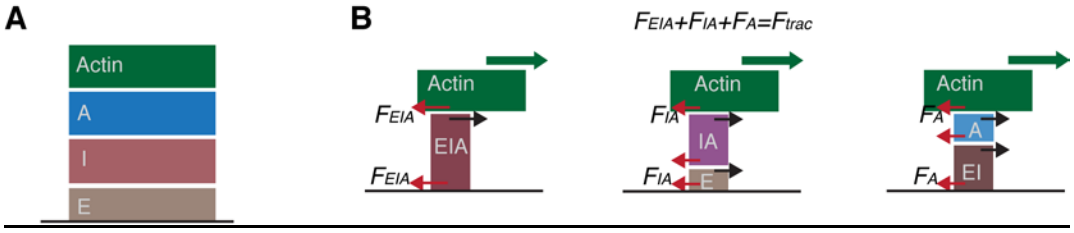

Figure S1. *Model scheme of force balance. (A) Schematized layered structure of focal adhesion and geometry of focal adhesion-actin flow interaction. (B) Force balance schemes for individual focal adhesion species. The green block arrows point to the downstream direction of actin flow. The red and the black arrows represent the reciprocal forces between the neighboring layers of focal adhesion.*
Left: The fully anchored ECM-Integrin-Adaptor (EIA); middle: Integrin-Adaptor (IA) and ECM (E); right: ECM-Integrin (EI) and Adaptor (A). The total traction force exerted upon the substrate is: $F_{trac}=F_{EIA}+F_{IA}+F_{A}$.

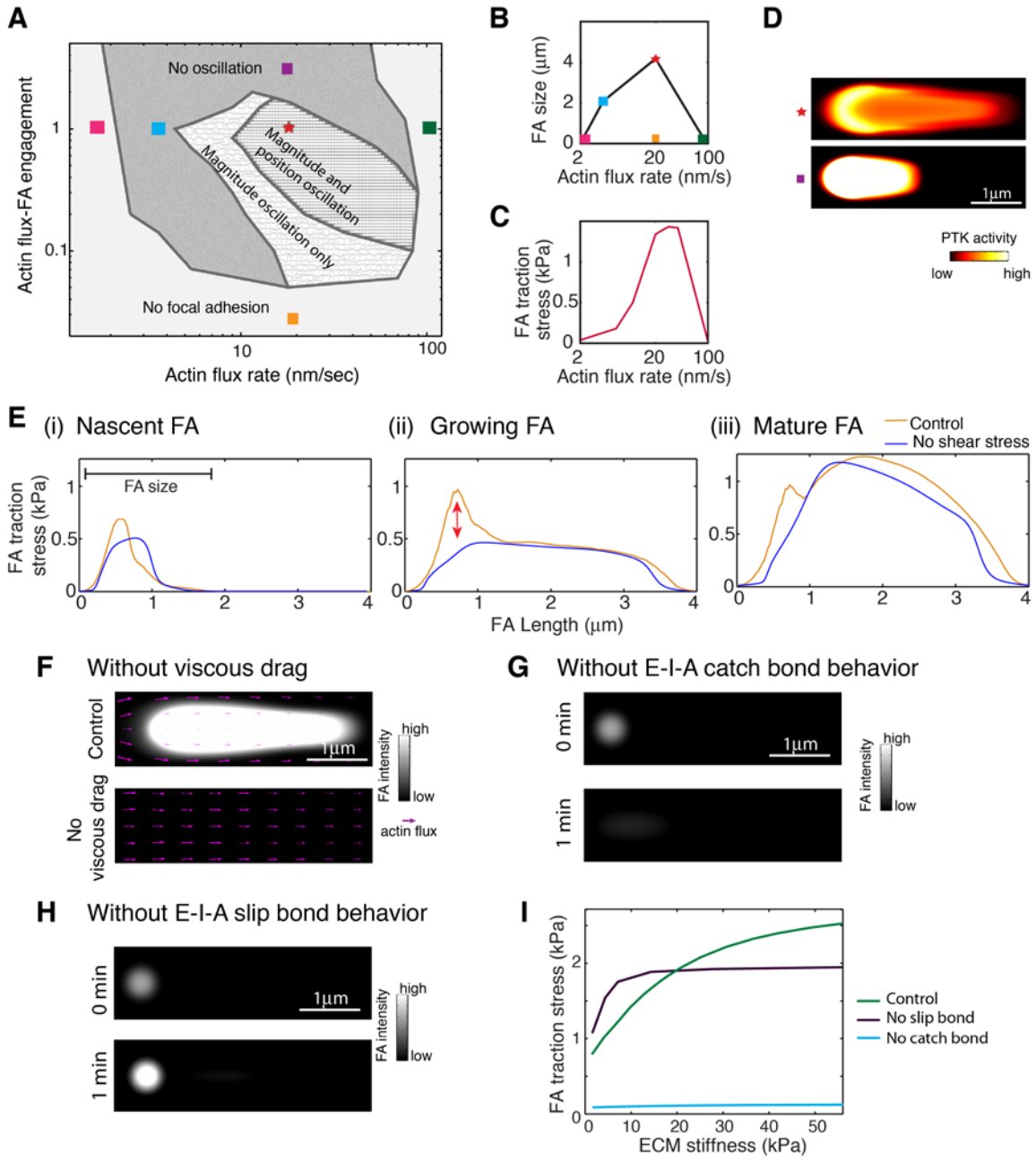

Figure S2 *Theoretical studies of the effects of FA-actin flux interaction on FA dynamics. (A) Phase diagram on the effects of actin retrograde flux velocity and actin-FA engagement on FA formation and traction oscillations. In the calculation, a constant factor is multiplied to the right hand side of the Eq. (S12) to modulate the FA engagement with the actin flux. This factor defines the y-axis, wherein the value of one corresponding to the nominal case. Different oscillation behaviors are indicated in the plot by different grey area. The red star represents the nominal case. The colored squares are different cases deviating from the nominal case. (B) FA size depends on actin flux velocity. The different styled markers correspond to the distinct conditions labeled on Fig S2(A). (C) Biphasic dependence of FA traction stress on actin flux velocity. (D) Snapshots of PTK activity distribution along an individual FA in response to change in actin-FA engagement. Upper panel shows PTK activity under nominal condition (control); lower panel shows PTK activity when actin-FA engagement is increased by 2 folds. Note, that stronger FA-actin flux engagement leads to a higher PTK activity within the FA, but also halts the growth of FA*

(lower panel) comparing to control (upper panel). (E) Snapshots of the FA traction stress profile evolving from nascent to matured FA. It compares the control (orange line) with the condition that there is no shear stress (blue line). (F) Snapshots of a typical model results on FA growth in the presence (upper panel) and in the absence (lower panel) of a viscous drag. Note, that in contrast to control, nascent FA disappears when the viscous drag coefficient ξ_0 *is set to zero. (G) Snapshots of a typical model result on FA temporal evolution in the absence of the catch bond behavior. Nascent FA vanishes when the E-I-A catch bond behavior is turned off, i.e.,* $k_{+F}^{(0)}$ *and* $k_{+F}^{(1)}$ *are set to zero. (H) Snapshots of a typical model results on FA temporal evolution in the absence of a slip bond. FA gets reinforced but fails to elongate when E-I-A slip bond behavior is turned off, i.e.,* $k_{-}^{(0)}$ *and* $k_{-}^{(1)}$ *are set to zero. (I) Model results on FA traction stress as the function of ECM stiffness in the cases of control (green), no slip bonds (purple) and no catch bonds (blue).*

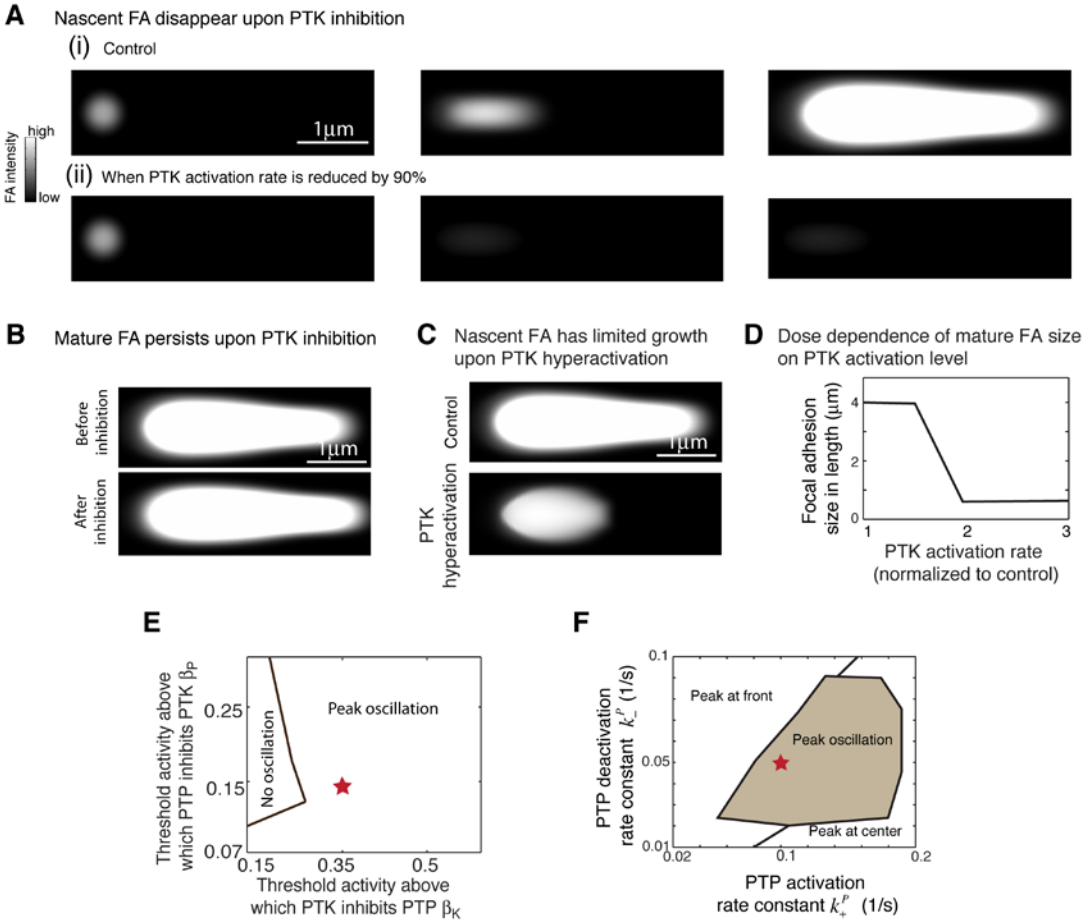

Figure S3 *Theoretical studies of the PTK-PTP mutual antagonism effects on FA dynamics. (A) Snapshots of FA profile when the PTK is inhibited from the nascent stage of the FA. (i) control. (ii) PTK on rate* k_+^K *is reduced to 10% of control. (B) Snapshots of a typical model results on the effect of PTK inhibition on a mature FA. Note that mature FA persists when PTK on rate* k_+^K *is reduced to 10% of the control. (C) Snapshots of a typical model results on the effect of PTK inhibition on a nascent FA. Nascent FA has limited growth when the PTK on rate is increased to 2 folds of the control. (D) The dose-dependence of mature FA size on the increase in the PTK on rate* k_+^K*. (E) Phase diagram of the dependence of FA traction peak oscillation on the mutual inhibition thresholds in PTK/PTP toggle switch (* β_K *and* β_P*). (F) Phase diagram of the dependence of FA traction peak oscillation on the PTP on and off rates (* k_+^P *and* k_-^P*).*

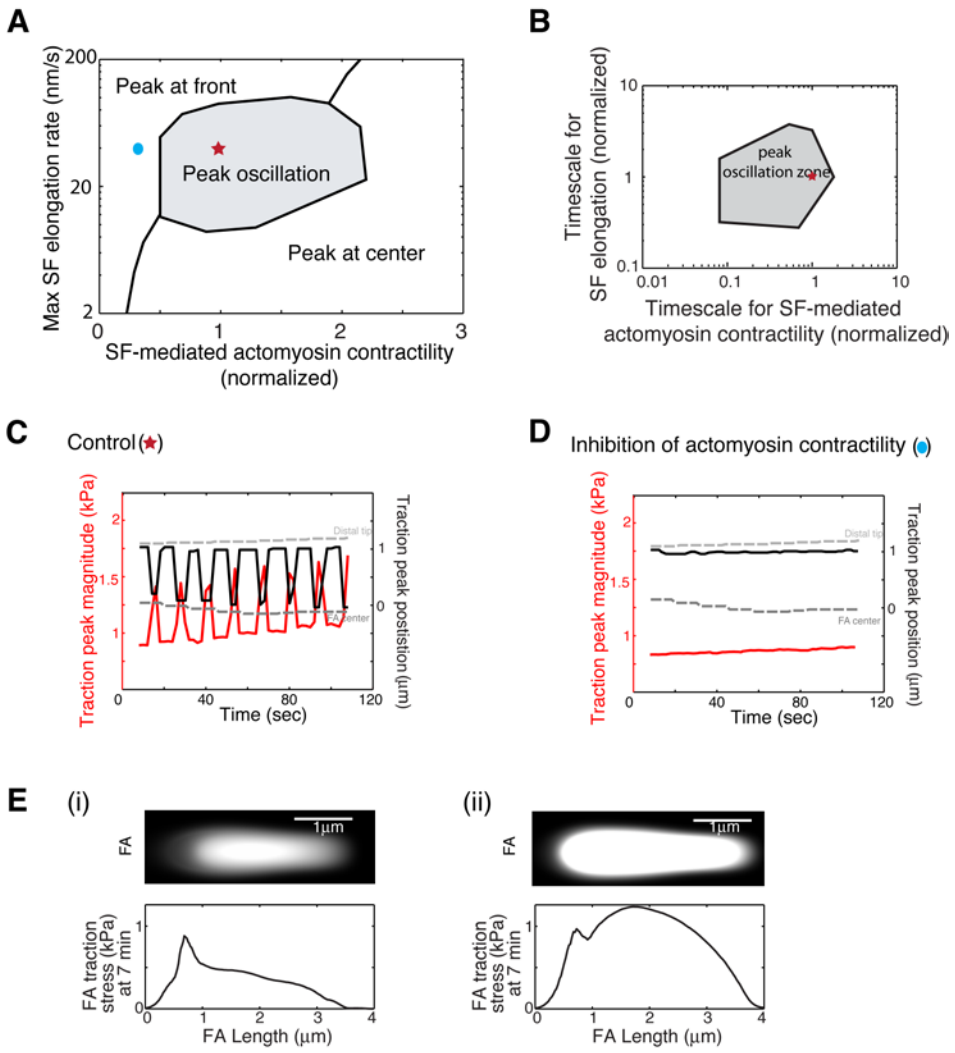

Figure S4 *Theoretical studies of the effects of stress fiber elongation and actomyosin contractility on FA dynamics. (A) Model phase diagram shows that traction peak oscillations exist in a broad and physiologically relevant range of SF-mediated actomyosin contractility and stress fiber elongation rate. In this calculation, we multiplied a constant factor to the right hand side of the Eq. (S16) to modulate the actomyosin contractility. This factor defines the x-axis; and it equals to one for the control (marked by the red star), whereas >1 and <1 represent the hyperactivation and the inhibition of actomyosin contractility (e.g., marked by the blue dot), respectively. (B) Model phase diagram shows that traction peak oscillation exists in a physiological range of the timescales for stress fiber elongation and actomyosin contractility. In this calculation, we multiplied different scale factors to the right hand side of the Eq. (S15) and (S17) to modulate the overall paces of the actomyosin contraction and the SF elongation, respectively. These two factors define the x-axis and the y-axis, which are normalized by the control (marked by the red star). (C) The model results show the time curves for the anti-phase oscillations of the FA traction peak magnitude and position for control. The gray dash lines indicate the FA distal tip and FA center, respectively. (D) The model results show that the traction peak stays at the FA distal tip and does not oscillate upon the inhibition of the actomyosin contractility inhibition (indicated by blue dot in (A)). (E) Effect of inhibiting SF formation on FA growth and traction force generation. (i) Model results of FA intensity profile and the traction profile at 7 min when the SF formation is disrupted by the actomyosin inhibition. (ii) The corresponding control case.*

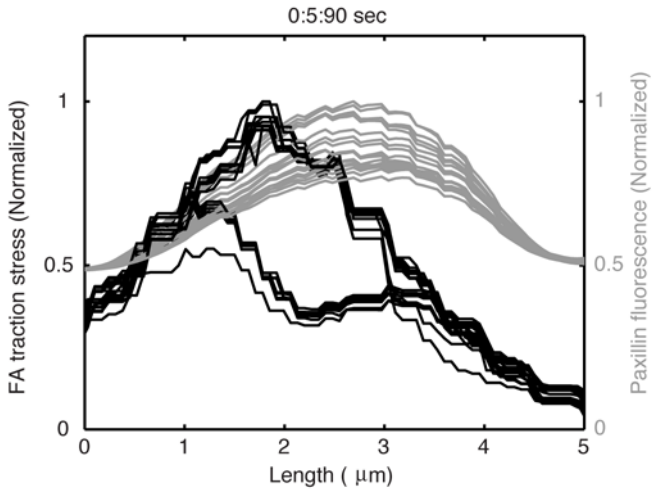

Figure S5 *Typical Snapshots of FA traction stress profiles (black lines) and the corresponding FA intensity profiles (paxillin fluorescence intensity, grey lines). The snapshot profiles were taken along the central line of FA over 90 sec with the time interval of 5 sec. In Figure 2D, the FA domains were calibrated for a better contrast by subtracting the paxillin fluorescence intensity (~ 0.55 in the normalized value) that is 10% higher than its background.*

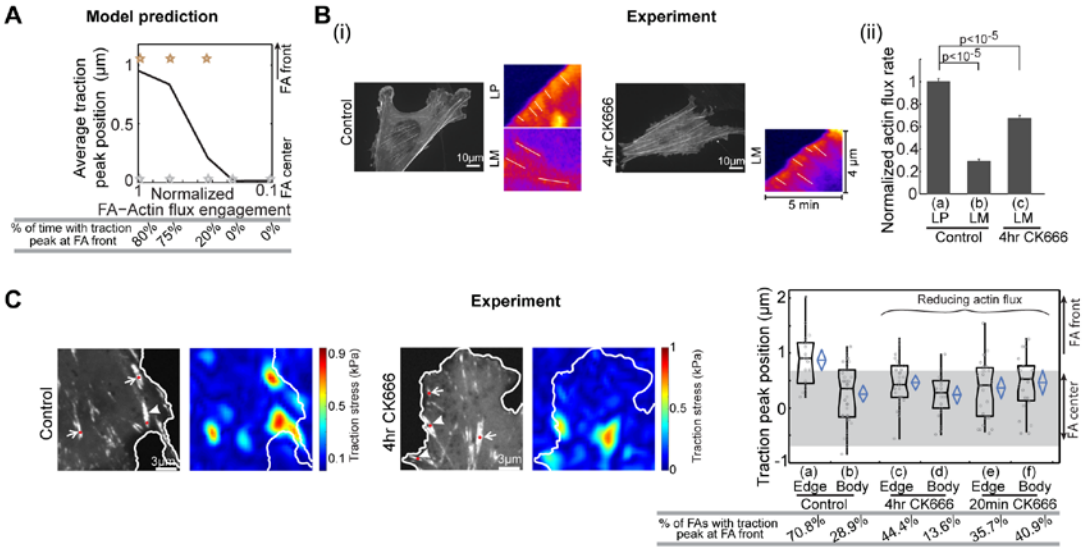

Figure S6 *Distal traction peak requires Arp2/3-mediated actin flux. (A) Predicted effect of actin fluxes on the magnitude of the distal traction peak and the overall location of the FA traction maximum. Above: Dependence of the position of the FA traction maximum on FA-actin flux engagement. Orange star: the distal traction peak location. Grey star: the central traction peak location. Solid black line: the time-averaged traction peak position during traction peak oscillation. Below: the fraction of time during which the FA traction maximum is at the FA distal end. (B) CK-666 treatment reduces the actin flux rate. (i) Representative experiment images for control cells and CK-666 treated cells and the kymographs of actin fluxes in cell lamellipodium (LP) and lamellum (LM). White lines indicate retrograde movement of actin network in cell LP and LM. Note that the cells treated with 100μM CK-666 for 4 hrs did not form LP. (ii) Quantification of actin flux rates in (i). Control: n=220 for the cell LP, and n=212 for the cell LM. CK-666 treatment: n=90 for the cell LM right behind the cell edge. Error bars: SEM. p values: student's t-test. (C) Experiments indicate that the actin retrograde flux contributes to the distal traction peak, but not to the central traction peak. Left and middle: Representative images of individual FAs marked by eGFP-paxillin and the corresponding TFM images for control cells and cells with 4-hour CK666 treatment, respectively. The red dots mark the respective traction maximum location for individual FAs. The arrowheads mark the FAs near the cell leading edge whereas the arrows mark the FAs deep inside the cell body. Right: (Above) boxplots of the peak traction position within individual FAs that have different sub-cellular localization. Columns (a-b): control (24 FAs located at the cell edges and 45 FAs deep inside the cell body). Columns (c-d): 4-hour CK-666 treated cells (37 FAs located at cell edge and 22 FAs located in cell body). Column (e-f): 20-min CK-666 treated cells (28 FAs located at cell edge and 22 FAs located in cell body). Each blue diamond represents the respective 95% confidence interval. (Below) the fraction of single FAs with traction maximum at FA distal end.*

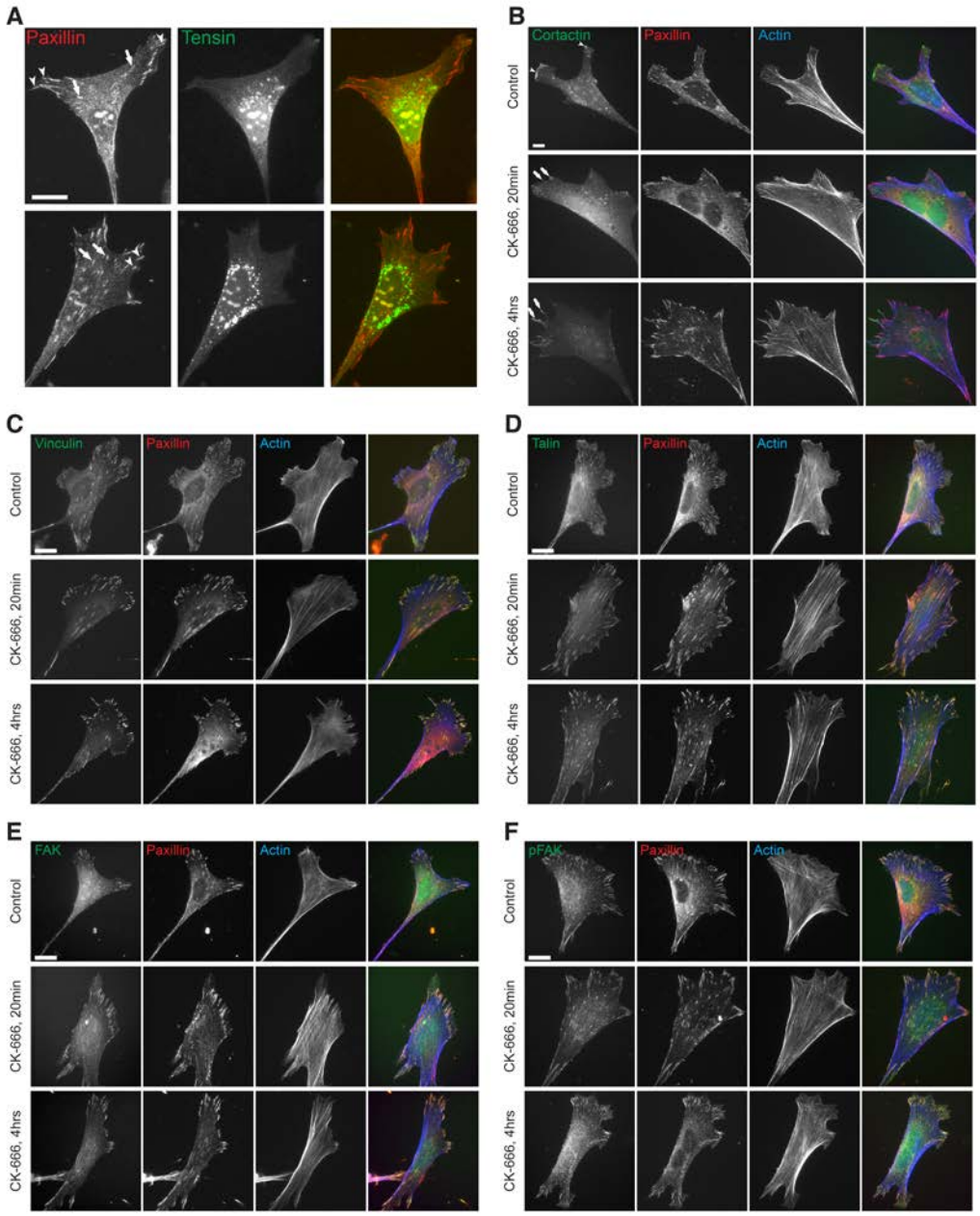

Figure S7 *Immunostaining images of cell adhesion markers. (A) Representative tensin immunofluorescent images of wild type MEFs. Note that both peripheral adhesions (indicated with arrowheads) and adhesions located towards the cell center (indicated with arrows) were negative for tensin. (B)-(F) Representative immunofluorescent images of control and CK-666 treated cells stained for cortactin, actin, paxillin, and other FA proteins. Bar, 10 μm.*

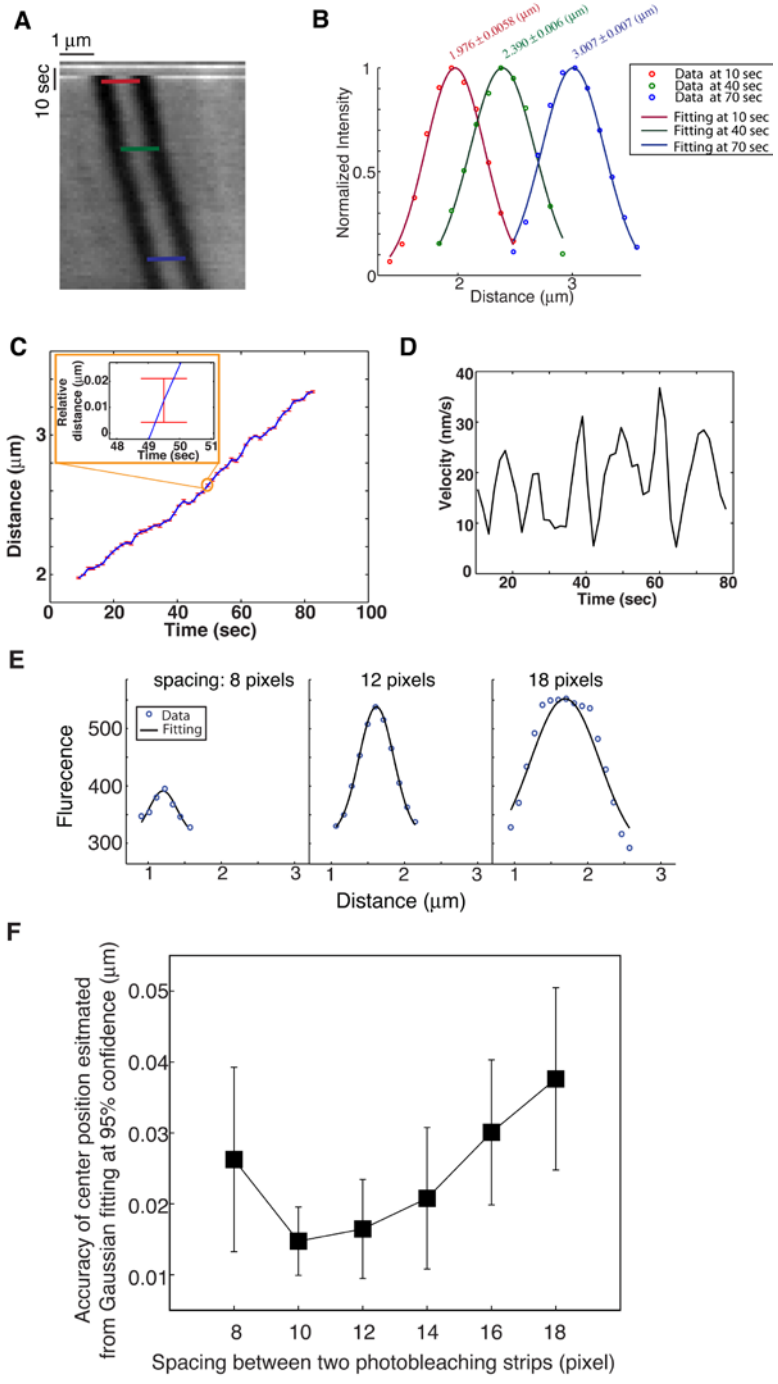

Figure S8 *Analysis on SF elongation rate oscillation as setup in Fig 3. (A) A typical kymograph of SF elongation with two photo-bleaching strips, and an bright photo-label was created in-between. The grey scale indicates the fluorescence of mCherry-actin. (B) Comparison between the measured intensity profiles of bright photo-labels (as indicated with red line in (A)) and the Gaussian fitting at different times after the photobleaching. With this fitting, one can approximate the mean position of the bright photo-label as the Gaussian center. The Gaussian fitting was implemented by standard nonlinear regression of Matlab Statistics toolbox. Fitting quality was shown above each dataset. (C) A typical time curve of the centroid position of the bright photo-label by the Gaussian fitting as in (B). The red error bar indicates the standard error of mean position, which is ~ 20 nm in accuracy as shown in the inset of (C). The confidence intervals were obtained by the regression parameter confidence interval estimator*

in Matlab Statistics toolbox. (D) A typical time curve of SF elongation velocity from calculating the slope at each position as in (C). (E-F) Accuracy analysis on determining the centroid position of the bright photo-label. (E) Comparisons between the intensity profiles of the bright photo-label obtained from the photobleaching experiments (blue circle) and the corresponding Gaussian fitting curve (black line). Three bandwidths (0.86 μm; 1.29 μm; 1.94 μm) are shown. (F) The Gaussian fitting accuracy in determining the centroid position of the photo-label depends on the bandwidth. Each pixel has the size of 108 nm. The error bar is the standard derivation from > 16 measurements for each data point. Note that, when the initial width of photo-label was too wide, the intensity profile of the bright band became "flat", and was difficult to fit a Gaussian curve, which dramatically decreases the accuracy of the center position estimation. On the other hand, if the initial width of the photo-label was too narrow, then the intensity of the photo-label became too dim to maintain stable profile due to thermal fluctuations. The analysis based Gaussian fitting show that the initial widths of the photo-label ~10-12 pixels give the best accuracy (Fig S8(F)). We therefore use 12-pixel spacing in the experiments unless otherwise mentioned.

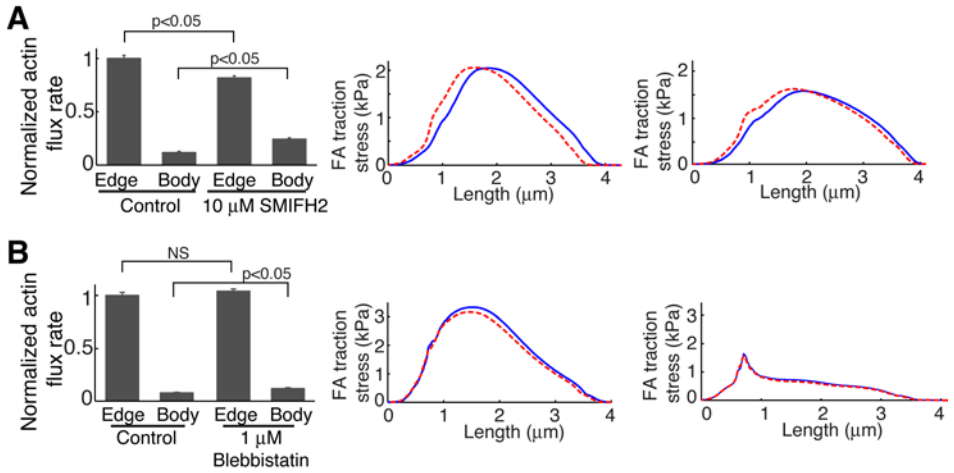

Figure S9 *Actin flux changes upon SMIFH2 and blebbistatin treatments. (A) SMIFH2 treatment. Left: Bar plot of normalized changes in actin flux rate upon formin inhibition by 10 μM SMIFH2. Control: 175 measurements at the cell leading edge from 10 cells; 105 measurements deep inside the cell body from 10 cells. 10 μM SMIFH2 treatment: 272 measurements at the cell leading edge from 12 cells; 168 measurements deep inside the cell body from 12 cells. Middle: Model predictions on the FA traction profile changes by only incorporating the actin flux changes evidenced in SMIFH2-mediated formin inhibition. Red line: the nominal case result without any perturbation on actin flux nor SF. Blue line: the calculation results that only incorporated the SMIFH2-mediated actin flux changes as measured and without considering the perturbation on SF. Right: Model predictions on the FA traction profile changes by incorporating the SMIFH2-caused changes in the actin flux, SF elongation rate and actomyosin contractility (Fig. 4 in the main text). Red line: the calculation result that was done by incorporating the changes in SF elongation rate and actomyosin contractility, without considering the SMIFH2-mediated actin flux changes. Blue line: the calculation result that quantitatively incorporated all the changes caused by the SMIFH2 treatment. For all the panels in (A), the ECM stiffness is 8.6 kPa. (B) Blebbistatin treatment. Left: Bar plot of normalized changes in actin flux rate upon inhibiting actomyosin contractility by 1 μM blebbistatin. Control: 103 measurements from 14 cells for LP/LM; 113 measurements from 14 cells for LM. 1 μM blebbistatin treatment: 385 measurements at the leading edge from 10 cells; 340 measurements deep inside the cell body from 10 cells. Middle: Model predictions on the FA traction profile changes by only incorporating the actin flux changes evidenced in blebbistatin-mediated actomyosin inhibition. Red line: the nominal case result without any perturbation on actin flux nor SF. Blue line: the calculation result that only incorporated the blebbistatin-mediated actin flux changes as measured and without considering the perturbation on SF. Right: Model predictions on FA traction profile changes by incorporating the blebbistatin caused-changes in the actin flux, SF elongation rate and actomyosin contractility (Fig. 4 in the main text). The results are shown at time = 7 min as above. Red line: the calculation result by incorporating the changes in SF elongation and actomyosin contractility, without considering the blebbistatin-mediated actin flux changes. Blue line: the calculation result by quantitatively incorporating all the blebbistatin-caused changes. For all the panels in (B), the ECM stiffness is 32 kPa. For the FA traction calculations in (A) and (B), the results are shown at time = 7 min, by which the FA was fully matured by engaging with both the actin flux and the SF. And because the traction peak is oscillating, we compared the traction profiles when the traction peaks reach their respective maximum. Error bar: SEM; p-values: student's t-test.*

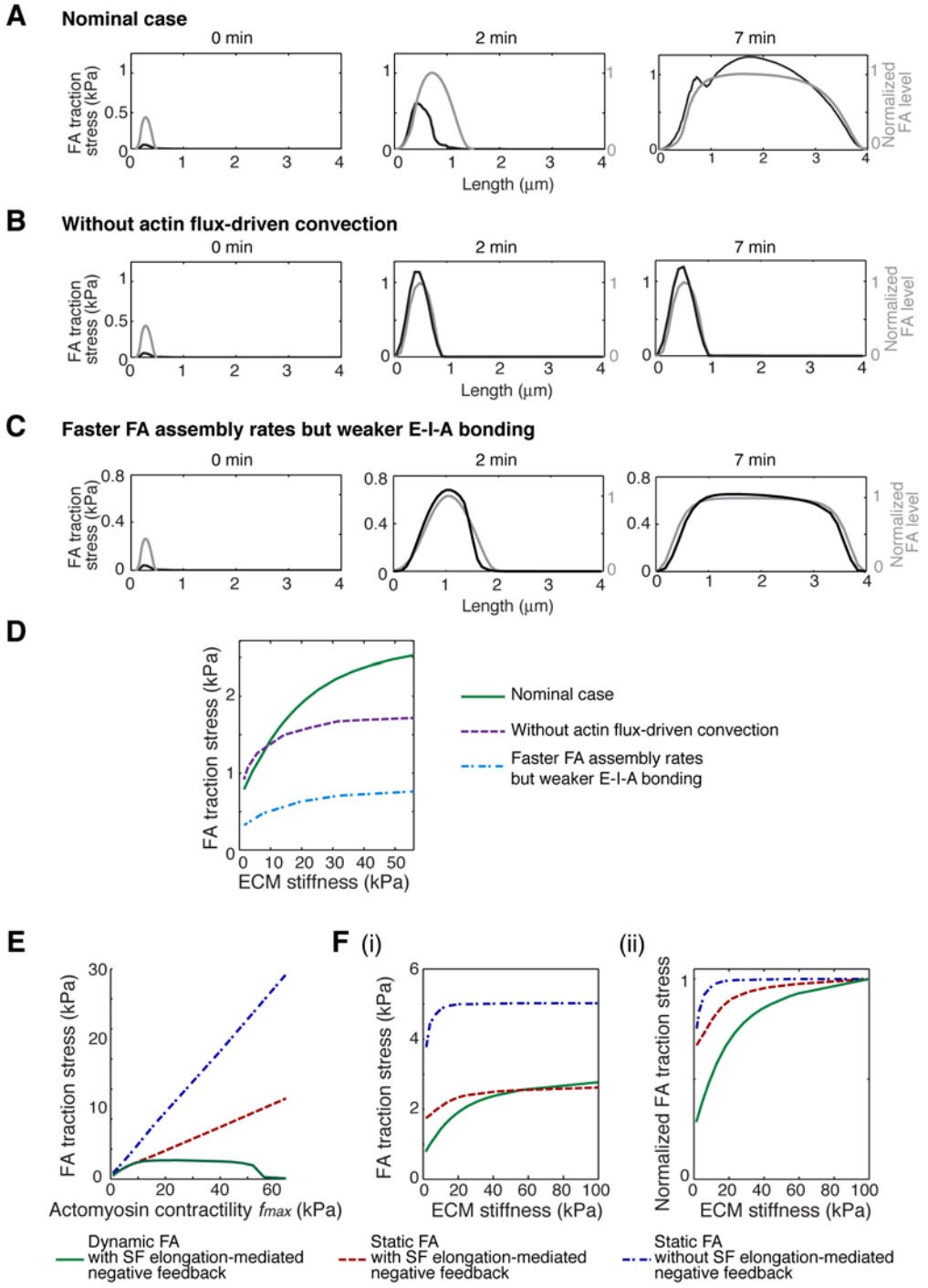

Figure S10 *FA-localized spatial-temporal dynamics arising from FA growth dictates mechanosensing. (A-C) Profiles of FA traction and intensity along the central line of FA domains over time (t=0, 2, and 7 min). (A): Nominal case; (B) Actin flux-driven convection of FA mobile components were completely turned off; (C) The overall rate of FA-localized chemical reactions were uniformly increased by 4 folds and the E–I–A bond strengths were uniformly decreased by 30%. (D) Dependence of FA traction stress on ECM stiffness at t = 7 min for (A-C). (E) Modulations of FA traction by actomyosin contractility. Please see Eq. (S16) for details of f_{max}. Green: Dynamic FA that preserves FA growth and SF elongation-mediated negative feedback. Red: Static FA with SF elongation-mediated negative feedback. Blue: Static FA without SF elongation-mediated negative feedback. (F) Dependence of FA traction stress on ECM*

stiffness. (i) Mechanosensing curves with absolute values of FA traction stress. (ii) Normalized mechanosensing curves. For each case, the FA traction stress was normalized by its respective maximum. In (E) and (F), the model first evolved FA from the nascent to maturation stage (t = 7 min) with the ECM stiffness =55 kPa and the nominal model parameter set (see Parameter Tables S1 and S2), including actomyosin contractility f_{max} = 8 kPa. From this mature FA, we further modulated actomyosin contractility in (E), and ECM stiffness in (F). For cases of static FAs, we then set all the reaction rates that directly involved in FA assembly to be zero for this mature FA and onward. This way, the FA profile, i.e., the spatial density profiles of FA components, was kept fixed against variations in actomyosin contractility, ECM stiffness, or SF elongation-mediated negative feedback. To mimic deprivation of SF elongation-mediated negative feedback, we set the SF elongation rate v_{n0} = 0 (see Eq. (S19)). For the case of dynamic FA, we preserved all of the FA-localized reaction rates as those in the nominal case. We note that the qualitative features predicted in (E) and (F) are insensitive to the choice of ECM stiffness and actomyosin contractility.

V. Supplemental References

1. Kanchanawong, P., G. Shtengel, A. M. Pasapera, E. B. Ramko, M. W. Davidson, H. F. Hess, and C. M. Waterman. 2010. Nanoscale architecture of integrin-based cell adhesions. Nature 468:580-584.
2. Tang, D., D. Mehta, and S. J. Gunst. 1999. Mechanosensitive tyrosine phosphorylation of paxillin and focal adhesion kinase in tracheal smooth muscle. American Journal of Physiology - Cell Physiology 276:C250-C258.
3. Sabass, B., and U. S. Schwarz. 2010. Modeling cytoskeletal flow over adhesion sites: competition between stochastic bond dynamics and intracellular relaxation. Journal of Physics: Condensed Matter 22:194112.
4. Giannone, G., B. J. Dubin-Thaler, H.-G. n. Dˆbereiner, N. Kieffer, A. R. Bresnick, and M. P. Sheetz. 2004. Periodic Lamellipodial Contractions Correlate with Rearward Actin Waves. Cell 116:431-443.
5. Hirata, H., H. Tatsumi, C. T. Lim, and M. Sokabe. 2014. Force-dependent vinculin binding to talin in live cells: a crucial step in anchoring the actin cytoskeleton to focal adhesions. Am J Physiol Cell Physiol 306:C607-C620.
6. del Rio, A., R. Perez-Jimenez, R. Liu, P. Roca-Cusachs, J. M. Fernandez, and M. P. Sheetz. 2009. Stretching Single Talin Rod Molecules Activates Vinculin Binding. Science 323:638-641.
7. Margadant, F., L. L. Chew, X. Hu, H. Yu, N. Bate, X. Zhang, and M. Sheetz. 2011. Mechanotransduction In Vivo by Repeated Talin Stretch-Relaxation Events Depends upon Vinculin. PLoS Biol 9:e1001223.
8. Hu, K., L. Ji, K. T. Applegate, G. Danuser, and C. M. Waterman-Storer. 2007. Differential Transmission of Actin Motion Within Focal Adhesions. Science 315:111-115.
9. Wachsstock, D. H., W. H. Schwarz, and T. D. Pollard. 1994. Cross-linker dynamics determine the mechanical properties of actin gels. Biophysical Journal 66:801-809.
10. Humphrey, D., C. Duggan, D. Saha, D. Smith, and J. Kas. 2002. Active fluidization of polymer networks through molecular motors. Nature 416:413-416.
11. Lieleg, O., M. M. A. E. Claessens, Y. Luan, and A. R. Bausch. 2008. Transient Binding and Dissipation in Cross-Linked Actin Networks. Physical Review Letters 101:108101.
12. Ward, S. M. V., A. Weins, M. R. Pollak, and D. A. Weitz. 2008. Dynamic Viscoelasticity of Actin Cross-Linked with Wild-Type and Disease-Causing Mutant α-Actinin-4. Biophysical Journal 95:4915-4923.
13. Lai, F. P., M. Szczodrak, J. Block, J. Faix, D. Breitsprecher, H. G. Mannherz, T. E. Stradal, G. A. Dunn, J. V. Small, and K. Rottner. 2008. Arp2/3 complex interactions and actin network turnover in lamellipodia. The EMBO Journal 27:982-992.
14. Fritzsche, M., A. Lewalle, T. Duke, K. Kruse, and G. Charras. 2013. Analysis of turnover dynamics of the submembranous actin cortex. Molecular Biology of the Cell 24:757-767.
15. Watanabe, N., and T. J. Mitchison. 2002. Single-Molecule Speckle Analysis of Actin Filament Turnover in Lamellipodia. Science 295:1083-1086.
16. Berret, J. F. 2016. Local viscoelasticity of living cells measured by rotational magnetic spectroscopy. Nat Commun 7.
17. Vallotton, P., S. L. Gupton, C. M. Waterman-Storer, and G. Danuser. 2004. Simultaneous mapping of filamentous actin flow and turnover in migrating cells by

quantitative fluorescent speckle microscopy. Proceedings of the National Academy of Sciences of the United States of America 101:9660-9665.
18. Pollard, T. D., and G. G. Borisy. 2003. Cellular Motility Driven by Assembly and Disassembly of Actin Filaments. Cell 112:453-465.
19. Zicha, D., I. M. Dobbie, M. R. Holt, J. Monypenny, D. Y. H. Soong, C. Gray, and G. A. Dunn. 2003. Rapid Actin Transport During Cell Protrusion. Science 300:142-145.
20. Fan, Y., S. M. Eswarappa, M. Hitomi, and P. L. Fox. 2012. Myo1c facilitates G-actin transport to the leading edge of migrating endothelial cells. The Journal of Cell Biology 198:47-55.
21. Kong, F., A. J. Garcia, A. P. Mould, M. J. Humphries, and C. Zhu. 2009. Demonstration of catch bonds between an integrin and its ligand. The Journal of Cell Biology 185:1275-1284.
22. Marshall, B. T., M. Long, J. W. Piper, T. Yago, R. P. McEver, and C. Zhu. 2003. Direct observation of catch bonds involving cell-adhesion molecules. Nature 423:190-193.
23. Bell, G. I. 1978. Models for the specific adhesion of cells to cells. Science 200:618-627.
24. Walcott, S., D.-H. Kim, D. Wirz, and S. X. Sun. 2011. Nucleation and Decay Initiation Are the Stiffness-Sensitive Phases of Focal Adhesion Maturation. Biophysical Journal 101:2919-2928.
25. Guilluy, C., R. Garcia-Mata, and K. Burridge. 2011. Rho protein crosstalk: another social network? Trends in Cell Biology 21:718-726.
26. Tomar, A., and D. D. Schlaepfer. 2009. Focal adhesion kinase: switching between GAPs and GEFs in the regulation of cell motility. Current Opinion in Cell Biology 21:676-683.
27. Yokoyama, N., and W. T. Miller. 2001. Protein phosphatase 2A interacts with the Src kinase substrate p130CAS. Oncogene 20:6057-6065.
28. Jamieson, J. S., D. A. Tumbarello, M. Halle, M. C. Brown, M. L. Tremblay, and C. E. Turner. 2005. Paxillin is essential for PTP-PEST-dependent regulation of cell spreading and motility: a role for paxillin kinase linker. J Cell Sci 118:5835-5847.
29. Walcott, S., and S. X. Sun. 2010. A mechanical model of actin stress fiber formation and substrate elasticity sensing in adherent cells. Proceedings of the National Academy of Sciences 107:7757-7762.
30. Choi, C. K., J. Zareno, M. A. Digman, E. Gratton, and A. R. Horwitz. 2011. Cross-Correlated Fluctuation Analysis Reveals Phosphorylation-Regulated Paxillin-FAK Complexes in Nascent Adhesions. Biophysical Journal 100:583-592.
31. Pasapera, A. M., I. C. Schneider, E. Rericha, D. D. Schlaepfer, and C. M. Waterman. 2010. Myosin II activity regulates vinculin recruitment to focal adhesions through FAK-mediated paxillin phosphorylation. The Journal of Cell Biology 188:877-890.
32. Goldmann, W. H., Z. Guttenberg, J. X. Tang, K. Kroy, G. Isenberg, and R. M. Ezzell. 1998. Analysis of the F-actin binding fragments of vinculin using stopped-flow and dynamic light-scattering measurements. European Journal of Biochemistry 254:413-419.
33. Brami‐Cherrier, K., N. Gervasi, D. Arsenieva, K. Walkiewicz, M. C. Boutterin, A. Ortega, P. G. Leonard, B. Seantier, L. Gasmi, T. Bouceba, G. Kadaré, J. A. Girault, and S. T. Arold. 2014. FAK dimerization controls its kinase‐dependent functions at focal adhesions. The EMBO Journal.
34. Courtemanche, N., J. Y. Lee, T. D. Pollard, and E. C. Greene. 2013. Tension modulates actin filament polymerization mediated by formin and profilin. Proceedings of the National Academy of Sciences.

35. Jégou, A., M.-F. Carlier, and G. Romet-Lemonne. 2013. Formin mDia1 senses and generates mechanical forces on actin filaments. Nat Commun 4:1883.
36. Hansen, S. D., and R. D. Mullins. 2010. VASP is a processive actin polymerase that requires monomeric actin for barbed end association. The Journal of Cell Biology 191:571-584.
37. Bustamante, C., Y. R. Chemla, N. R. Forde, and D. Izhaky. 2004. MECHANICAL PROCESSES IN BIOCHEMISTRY. Annual Review of Biochemistry 73:705-748.
38. Shemesh, T., T. Otomo, M. K. Rosen, A. D. Bershadsky, and M. M. Kozlov. 2005. A novel mechanism of actin filament processive capping by formin: solution of the rotation paradox. The Journal of Cell Biology 170:889-893.
39. Xu, Y., J. B. Moseley, I. Sagot, F. Poy, D. Pellman, B. L. Goode, and M. J. Eck. 2004. Crystal Structures of a Formin Homology-2 Domain Reveal a Tethered Dimer Architecture. Cell 116:711-723.
40. Otomo, T., D. R. Tomchick, C. Otomo, S. C. Panchal, M. Machius, and M. K. Rosen. 2005. Structural basis of actin filament nucleation and processive capping by a formin homology 2 domain. Nature 433:488-494.
41. Zumdieck, A., K. Kruse, H. Bringmann, A. A. Hyman, and F. Jülicher. 2007. Stress Generation and Filament Turnover during Actin Ring Constriction. PLoS ONE 2:e696.
42. Kumar, S., I. Z. Maxwell, A. Heisterkamp, T. R. Polte, T. P. Lele, M. Salanga, E. Mazur, and D. E. Ingber. 2006. Viscoelastic Retraction of Single Living Stress Fibers and Its Impact on Cell Shape, Cytoskeletal Organization, and Extracellular Matrix Mechanics. Biophysical Journal 90:3762-3773.
43. Deguchi, S., T. Ohashi, and M. Sato. 2006. Tensile properties of single stress fibers isolated from cultured vascular smooth muscle cells. Journal of biomechanics 39:2603-2610.
44. Patla, I., T. Volberg, N. Elad, V. Hirschfeld-Warneken, C. Grashoff, R. Fassler, J. P. Spatz, B. Geiger, and O. Medalia. 2010. Dissecting the molecular architecture of integrin adhesion sites by cryo-electron tomography. Nat Cell Biol 12:909-915.
45. Hotulainen, P., and P. Lappalainen. 2006. Stress fibers are generated by two distinct actin assembly mechanisms in motile cells. The Journal of Cell Biology 173:383-394.
46. Nguyen, T. N., A. Uemura, W. Shih, and S. Yamada. 2010. Zyxin-mediated Actin Assembly Is Required for Efficient Wound Closure. Journal of Biological Chemistry 285:35439-35445.
47. Drees, B., E. Friederich, J. Fradelizi, D. Louvard, M. C. Beckerle, and R. M. Golsteyn. 2000. Characterization of the Interaction between Zyxin and Members of the Ena/Vasodilator-stimulated Phosphoprotein Family of Proteins. Journal of Biological Chemistry 275:22503-22511.
48. Lele, T. P., J. Pendse, S. Kumar, M. Salanga, J. Karavitis, and D. E. Ingber. 2006. Mechanical forces alter zyxin unbinding kinetics within focal adhesions of living cells. Journal of Cellular Physiology 207:187-194.
49. Kühnel, K., T. Jarchau, E. Wolf, I. Schlichting, U. Walter, A. Wittinghofer, and S. V. Strelkov. 2004. The VASP tetramerization domain is a right-handed coiled coil based on a 15-residue repeat. Proceedings of the National Academy of Sciences of the United States of America 101:17027-17032.
50. Kovács, M., K. Thirumurugan, P. J. Knight, and J. R. Sellers. 2007. Load-dependent mechanism of nonmuscle myosin 2. Proceedings of the National Academy of Sciences 104:9994-9999.

51. Saez, A., A. Buguin, P. Silberzan, and B. Æ. Ladoux. 2005. Is the Mechanical Activity of Epithelial Cells Controlled by Deformations or Forces? Biophysical Journal 89:L52-L54.
52. Ghibaudo, M., A. Saez, L. Trichet, A. Xayaphoummine, J. Browaeys, P. Silberzan, A. Buguin, and B. Ladoux. 2008. Traction forces and rigidity sensing regulate cell functions. Soft Matter 4:1836-1843.
53. Bruinsma, R., A. Behrisch, and E. Sackmann. 2000. Adhesive switching of membranes: Experiment and theory. Physical Review E 61:4253-4267.
54. Simson, R., E. Wallraff, J. Faix, J. Niewˆhner, G. n. Gerisch, and E. Sackmann. 1998. Membrane Bending Modulus and Adhesion Energy of Wild-Type and Mutant Cells of Dictyostelium Lacking Talin or Cortexillins. Biophysical Journal 74:514-522.
55. Bausch, A. R., F. Ziemann, A. A. Boulbitch, K. Jacobson, and E. Sackmann. 1998. Local Measurements of Viscoelastic Parameters of Adherent Cell Surfaces by Magnetic Bead Microrheometry. Biophysical Journal 75:2038-2049.
56. Taubenberger, A., D. A. Cisneros, J. Friedrichs, P.-H. Puech, D. J. Muller, and C. M. Franz. 2007. Revealing Early Steps of α2β1 Integrin-mediated Adhesion to Collagen Type I by Using Single-Cell Force Spectroscopy. Molecular Biology of the Cell 18:1634-1644.
57. Wenger, M. P. E., L. Bozec, M. A. Horton, and P. Mesquida. 2007. Mechanical Properties of Collagen Fibrils. Biophysical Journal 93:1255-1263.
58. Wiseman, P. W., C. M. Brown, D. J. Webb, B. Hebert, N. L. Johnson, J. A. Squier, M. H. Ellisman, and A. F. Horwitz. 2004. Spatial mapping of integrin interactions and dynamics during cell migration by Image Correlation Microscopy. Journal of Cell Science 117:5521-5534.
59. Rossier, O., V. Octeau, J.-B. Sibarita, C. c. Leduc, B. a. Tessier, D. Nair, V. Gatterdam, O. Destaing, C. Albig√ ®s-Rizo, R. Tamp√ ©, L. Cognet, D. Choquet, B. Lounis, and G. g. Giannone. 2012. Integrins β1 and β3 exhibit distinct dynamic nanoscale organizations inside focal adhesions. Nat Cell Biol 14:1057-1067.
60. Matthews, B. D., D. R. Overby, F. J. Alenghat, J. Karavitis, Y. Numaguchi, P. G. Allen, and D. E. Ingber. 2004. Mechanical properties of individual focal adhesions probed with a magnetic microneedle. Biochemical and Biophysical Research Communications 313:758-764.
61. Abraham, V. C., V. Krishnamurthi, D. L. Taylor, and F. Lanni. 1999. The Actin-Based Nanomachine at the Leading Edge of Migrating Cells. Biophysical Journal 77:1721-1732.
62. Thievessen, I., P. M. Thompson, S. Berlemont, K. M. Plevock, S. V. Plotnikov, A. Zemljic-Harpf, R. S. Ross, M. W. Davidson, G. Danuser, S. L. Campbell, and C. M. Waterman. 2013. Vinculin,Äìactin interaction couples actin retrograde flow to focal adhesions, but is dispensable for focal adhesion growth. The Journal of Cell Biology 202:163-177.
63. Litvinov, R. I., A. Mekler, H. Shuman, J. S. Bennett, V. Barsegov, and J. W. Weisel. 2012. Resolving Two-dimensional Kinetics of the Integrin Œ±IIbŒ≤3-Fibrinogen Interactions Using Binding-Unbinding Correlation Spectroscopy. Journal of Biological Chemistry 287:35275-35285.
64. Ponti, A., M. Machacek, S. L. Gupton, C. M. Waterman-Storer, and G. Danuser. 2004. Two Distinct Actin Networks Drive the Protrusion of Migrating Cells. Science 305:1782-1786.
65. Choi, C. K., M. Vicente-Manzanares, J. Zareno, L. A. Whitmore, A. Mogilner, and A. R. Horwitz. 2008. Actin and [alpha]-actinin orchestrate the assembly and maturation

of nascent adhesions in a myosin II motor-independent manner. Nat Cell Biol 10:1039-1050.
66. Legate, K. R., S. Takahashi, N. Bonakdar, B. Fabry, D. Boettiger, R. Zent, and R. Fassler. 2011. Integrin adhesion and force coupling are independently regulated by localized PtdIns(4,5)2 synthesis. EMBO J 30:4539-4553.
67. Wolfenson, H., A. Bershadsky, Y. I. Henis, and B. Geiger. 2011. Actomyosin-generated tension controls the molecular kinetics of focal adhesions. Journal of Cell Science 124:1425-1432.
68. Lele, T. P., C. K. Thodeti, J. Pendse, and D. E. Ingber. 2008. Investigating complexity of protein-protein interactions in focal adhesions. Biochemical and Biophysical Research Communications 369:929-934.
69. Grashoff, C., B. D. Hoffman, M. D. Brenner, R. Zhou, M. Parsons, M. T. Yang, M. A. McLean, S. G. Sligar, C. S. Chen, T. Ha, and M. A. Schwartz. 2010. Measuring mechanical tension across vinculin reveals regulation of focal adhesion dynamics. Nature 466:263-266.
70. Sawada, Y., M. Tamada, B. J. Dubin-Thaler, O. Cherniavskaya, R. Sakai, S. Tanaka, and M. P. Sheetz. 2006. Force Sensing by Mechanical Extension of the Src Family Kinase Substrate p130Cas. Cell 127:1015-1026.
71. Cai, X., D. Lietha, D. F. Ceccarelli, A. V. Karginov, Z. Rajfur, K. Jacobson, K. M. Hahn, M. J. Eck, and M. D. Schaller. 2008. Spatial and Temporal Regulation of Focal Adhesion Kinase Activity in Living Cells. Molecular and Cellular Biology 28:201-214.
72. Plotnikov, S. V., A. M. Pasapera, B. Sabass, and C. M. Waterman. 2012. Force Fluctuations within Focal Adhesions Mediate ECM-Rigidity Sensing to Guide Directed Cell Migration. Cell 151:1513-1527.
73. Tan, J. L., J. Tien, D. M. Pirone, D. S. Gray, K. Bhadriraju, and C. S. Chen. 2003. Cells lying on a bed of microneedles: An approach to isolate mechanical force. Proceedings of the National Academy of Sciences 100:1484-1489.
74. Geeves, M., H. Griffiths, S. Mijailovich, and D. Smith. 2011. Cooperative [Ca2+]-Dependent Regulation of the Rate of Myosin Binding to Actin: Solution Data and the Tropomyosin Chain Model. Biophysical Journal 100:2679-2687.
75. Nagy, A., Y. Takagi, N. Billington, S. A. Sun, D. K. T. Hong, E. Homsher, A. Wang, and J. R. Sellers. 2013. Kinetic Characterization of Nonmuscle Myosin IIB at the Single Molecule Level. Journal of Biological Chemistry 288:709-722.
76. Thoresen, T., M. Lenz, and Margaret L. Gardel. 2013. Thick Filament Length and Isoform Composition Determine Self-Organized Contractile Units in Actomyosin Bundles. Biophysical Journal 104:655-665.
77. Rosenfeld, S. S., J. Xing, L.-Q. Chen, and H. L. Sweeney. 2003. Myosin IIB Is Unconventionally Conventional. Journal of Biological Chemistry 278:27449-27455.
78. Butler, B., C. Gao, A. T. Mersich, and S. D. Blystone. 2006. Purified Integrin Adhesion Complexes Exhibit Actin-Polymerization Activity. Current Biology 16:242-251.
79. Kuhn, J. R., and T. D. Pollard. 2005. Real-Time Measurements of Actin Filament Polymerization by Total Internal Reflection Fluorescence Microscopy. Biophysical Journal 88:1387-1402.
80. Rizvi, S. A., E. M. Neidt, J. Cui, Z. Feiger, C. T. Skau, M. L. Gardel, S. A. Kozmin, and D. R. Kovar. 2009. Identification and Characterization of a Small Molecule Inhibitor of Formin-Mediated Actin Assembly. Chemistry & Biology 16:1158-1168.
81. Critchley, D. R. 2009. Biochemical and Structural Properties of the Integrin-Associated Cytoskeletal Protein Talin. Annual Review of Biophysics 38:235-254.

82. Ciobanasu, C., B. Faivre, and C. Le Clainche. 2014. Actomyosin-dependent formation of the mechanosensitive talin–vinculin complex reinforces actin anchoring. Nat Commun 5.
83. Zhu, J., B.-H. Luo, T. Xiao, C. Zhang, N. Nishida, and T. A. Springer. 2008. Structure of a Complete Integrin Ectodomain in a Physiologic Resting State and Activation and Deactivation by Applied Forces. Molecular Cell 32:849-861.
84. Zamir, E., M. Katz, Y. Posen, N. Erez, K. M. Yamada, B.-Z. Katz, S. Lin, D. C. Lin, A. Bershadsky, Z. Kam, and B. Geiger. 2000. Dynamics and segregation of cell-matrix adhesions in cultured fibroblasts. Nat Cell Biol 2:191-196.
85. Koestler, S. A., A. Steffen, M. Nemethova, M. Winterhoff, N. Luo, J. M. Holleboom, J. Krupp, S. Jacob, M. Vinzenz, F. Schur, K. Schlüter, P. W. Gunning, C. Winkler, C. Schmeiser, J. Faix, T. E. B. Stradal, J. V. Small, and K. Rottner. 2013. Arp2/3 complex is essential for actin network treadmilling as well as for targeting of capping protein and cofilin. Molecular Biology of the Cell 24:2861-2875.
86. Wu, C., Sreeja B. Asokan, Matthew E. Berginski, Elizabeth M. Haynes, Norman E. Sharpless, Jack D. Griffith, Shawn M. Gomez, and James E. Bear. 2012. Arp2/3 Is Critical for Lamellipodia and Response to Extracellular Matrix Cues but Is Dispensable for Chemotaxis. Cell 148:973-987.
87. Gardel, M. L., B. Sabass, L. Ji, G. Danuser, U. S. Schwarz, and C. M. Waterman. 2008. Traction stress in focal adhesions correlates biphasically with actin retrograde flow speed. The Journal of Cell Biology 183:999-1005.
88. Oakes, P. W., Y. Beckham, J. Stricker, and M. L. Gardel. 2012. Tension is required but not sufficient for focal adhesion maturation without a stress fiber template. The Journal of Cell Biology 196:363-374.
89. Webb, D. J., K. Donais, L. A. Whitmore, S. M. Thomas, C. E. Turner, J. T. Parsons, and A. F. Horwitz. 2004. FAK-Src signalling through paxillin, ERK and MLCK regulates adhesion disassembly. Nat Cell Biol 6:154-161.
90. Laukaitis, C. M., D. J. Webb, K. Donais, and A. F. Horwitz. 2001. Differential Dynamics of α5 Integrin, Paxillin, and α-Actinin during Formation and Disassembly of Adhesions in Migrating Cells. J. Cell Biol. 153:1427-1440.
91. Digman, M. A., C. M. Brown, A. R. Horwitz, W. W. Mantulin, and E. Gratton. 2008. Paxillin Dynamics Measured during Adhesion Assembly and Disassembly by Correlation Spectroscopy. Biophysical Journal 94:2819-2831.
92. Raz-Ben Aroush, D., R. Zaidel-Bar, A. D. Bershadsky, and H. D. Wagner. 2008. Temporal evolution of cell focal adhesions: experimental observations and shear stress profiles. Soft Matter 4:2410-2417.
93. Jiang, G., G. Giannone, D. R. Critchley, E. Fukumoto, and M. P. Sheetz. 2003. Two-piconewton slip bond between fibronectin and the cytoskeleton depends on talin. Nature 424:334-337.
94. Giannone, G., G. Jiang, D. H. Sutton, D. R. Critchley, and M. P. Sheetz. 2003. Talin1 is critical for force-dependent reinforcement of initial integrin-cytoskeleton bonds but not tyrosine kinase activation. J. Cell Biol. 163:409-419.
95. Alexandrova, A. Y., K. Arnold, S. b. Schaub, J. M. Vasiliev, J.-J. Meister, A. D. Bershadsky, and A. B. Verkhovsky. 2008. Comparative Dynamics of Retrograde Actin Flow and Focal Adhesions: Formation of Nascent Adhesions Triggers Transition from Fast to Slow Flow. PLoS ONE 3:e3234.
96. Carisey, A., R. Tsang, A. M. Greiner, N. Nijenhuis, N. Heath, A. Nazgiewicz, R. Kemkemer, B. Derby, J. Spatz, and C. Ballestrem. 2013. Vinculin Regulates the Recruitment and Release of Core Focal Adhesion Proteins in a Force-Dependent Manner. Current biology.

97. Michael, K. E., D. W. Dumbauld, K. L. Burns, S. K. Hanks, and A. J. García. 2009. Focal Adhesion Kinase Modulates Cell Adhesion Strengthening via Integrin Activation. Molecular Biology of the Cell 20:2508-2519.
98. Mitra, S. K., D. A. Hanson, and D. D. Schlaepfer. 2005. Focal adhesion kinase: in command and control of cell motility. Nat Rev Mol Cell Biol 6:56-68.
99. Wang, H.-B., M. Dembo, S. K. Hanks, and Y.-l. Wang. 2001. Focal adhesion kinase is involved in mechanosensing during fibroblast migration. Proceedings of the National Academy of Sciences 98:11295-11300.
100. Shi, Q., and D. Boettiger. 2003. A Novel Mode for Integrin-mediated Signaling: Tethering Is Required for Phosphorylation of FAK Y397. Molecular Biology of the Cell 14:4306-4315.
101. Ren, X. D., W. B. Kiosses, D. J. Sieg, C. A. Otey, D. D. Schlaepfer, and M. A. Schwartz. 2000. Focal adhesion kinase suppresses Rho activity to promote focal adhesion turnover. Journal of Cell Science 113:3673-3678.
102. Deramaudt, T. B., D. Dujardin, A. Hamadi, F. Noulet, K. Kolli, J. De Mey, K. Takeda, and P. Rondé. 2011. FAK phosphorylation at Tyr-925 regulates cross-talk between focal adhesion turnover and cell protrusion. Molecular Biology of the Cell 22:964-975.
103. Lawson, C., S.-T. Lim, S. Uryu, X. L. Chen, D. A. Calderwood, and D. D. Schlaepfer. 2012. FAK promotes recruitment of talin to nascent adhesions to control cell motility. The Journal of Cell Biology 196:223-232.